Chapter 1
Nanocrystalline Spinel Catalysts for Volatile Organic Compounds Abatement

Adriana Urdă, Ionel Popescu, and Ioan-Cezar Marcu

1.1 Introduction

Volatile organic compounds (VOC) are chemicals with relatively low molecular weight and high vapor pressure at normal temperatures, which are emitted into atmosphere from many sources [1]. Since they are linked to global environmental problems (e.g., photochemical smog, stratospheric ozone depletion, formation of tropospheric ozone), and also to health problems such as toxicity and carcinogenicity [2], their presence in atmosphere is monitored and regulated and their emission is controlled by different conventional or emerging methods [1, 3, 4], such as adsorption, scrubbing, and oxidation processes (thermal, catalytic, etc.).

Due to their net advantages, the catalytic processes are widely used for the abatement of VOC [1, 5–8]. In order to be able to convert VOC from gases with dilute levels of such compounds, the catalysts need to be both very active and selective [2]. Most industrial scale applications use noble metals (Pt, Pd) with high activity for the catalytic combustion of VOC [1], but because of their price, high sintering rate, and sensitivity to poisoning, many efforts are dedicated to the research of metal oxide catalysts that could be able to replace them [5, 8]. Indeed, a high number of research papers have been published on this subject, leading, in the last decade, to several review papers and book chapters focusing either on catalytic combustion of VOC [2,

A. Urdă · I.-C. Marcu (✉)
Laboratory of Chemical Technology and Catalysis, Department of Organic Chemistry, Biochemistry and Catalysis, Faculty of Chemistry, University of Bucharest, Bucharest, Romania

Research Center for Catalysts and Catalytic Processes, Faculty of Chemistry, University of Bucharest, Bucharest, Romania
e-mail: ioancezar.marcu@chimie.unibuc.ro

I. Popescu
Research Center for Catalysts and Catalytic Processes, Faculty of Chemistry, University of Bucharest, Bucharest, Romania

M. Piumetti, S. Bensaid (eds.), *Nanostructured Catalysts for Environmental Applications*, https://doi.org/10.1007/978-3-030-58934-9_1

9–11] and methane [12], or on different types of oxide catalysts, such as mesoporous silica-supported catalysts [13], ordered porous transition metal oxides [14], cobalt oxides [15], pillared clays [16, 17], and layered double hydroxide-derived mixed oxides [18]. Although the number of papers reporting spinel-based catalysts for total oxidation constantly increased in the last decade, only two review papers contain sections dedicated to them [10, 12].

Oxide spinels are magnesium aluminate ($MgAl_2O_4$)-related mixed oxides with the general formula AB_2O_4, with cations A and B located in tetrahedral and octahedral interstices of the cubic close-packed lattice of oxide anions [19]. The A cations can be all located in tetrahedral sites (normal spinels), in octahedral sites (inverse spinels), or they can be distributed between these two types of sites (random spinels) [19] depending on the cation size, covalent bonding effects, and crystal field stabilization energies. Spinels are used in numerous applications, among others, as magnetic materials [20–23], electronic equipment [24, 25], materials for solid oxide fuel cells [26], gas sensors [27], photocatalysts [28–31], or adsorbents [32, 33] for the removal of contaminants from water, catalysts [6, 23, 34–39], and cores for magnetically separable catalytic materials [23, 40, 41]. Catalytic combustion [5, 42, 43], water gas-shift reaction (WGS) [23], methanol or ethanol reforming [23, 44, 45], oxidative dehydrogenation of alkenes [46, 47], hydrocarbon selective oxidation [23, 34, 48], oxidative coupling of methane [43], esterification [49], CO oxidation [23, 50–53], selective reduction [54], N_2O decomposition [55], and water photoreduction [56, 57] represent reactions catalyzed by spinel compounds. Among this type of solids, ferrospinels (AFe_2O_4), manganites (AMn_2O_4), and cobaltites (ACo_2O_4) attracted most interest in the catalytic combustion of VOC. The recent achievements in the design and preparation of these spinel-based materials in correlation with their main physicochemical characteristics and the consequences on their catalytic performance in complete oxidation of VOC are discussed below through the most relevant examples from the literature published in the last decade.

1.2 Iron-Based Spinel Catalysts

According to their crystalline structure, ferrites can be classified into hexagonal ($MFe_{12}O_{19}$), garnet ($M_3Fe_5O_{12}$), spinel (MFe_2O_4, where M is a divalent, usually transition metal, e.g., Fe, Co, Ni, Cu, Mn, Zn), and orthoferrite ($REFeO_3$, where RE is a rare earth cation) compounds [23, 33].

Most spinel ferrites have a structure between normal and inverse spinel lattice, the structural formula being usually written as $\left(M^{2+}_{1-c}Fe^{3+}_{c}\right)\left[M^{2+}_{c}Fe^{3+}_{2-c}\right]O^{2-}_{4}$, where c represents the degree of inversion (the fraction of tetrahedral sites occupied by Fe^{3+} cations), the round brackets denote tetrahedral (A) sites, while the square brackets show the octahedral (B) sites [58].

Ferrites, both doped and undoped, are studied for the total oxidation of VOC due to their redox ability and stability in oxidative conditions [38, 59, 60]. A mini-review

discussing their preparation and applications, mainly for organic reactions, has been recently published by Kharisov et al. [23].

Many organic compounds were tested in catalytic combustion reactions catalyzed by spinel ferrites: methane [42, 43, 61, 62], ethane [63], propane [5, 7, 8, 64], propene [65], butane [63], 1-butene [65], acetone [7, 66], ethanol [60], and aromatics such as benzene [7] and toluene [4, 35, 67].

Magnetite, Fe_3O_4, has an inverse spinel structure, with the 32 oxygen anions forming a close-packed cubic lattice, and the iron cations placed both in 8 of the 64 tetrahedral (A) and 16 of the 32 octahedral (B) sites [23, 25]. It can be represented by the formula: $Fe^{3+}\left[Fe^{2+}_{1-y}Fe^{3+}_{1-y}Fe^{3+}_{1.67y}V_{0.33y}\right]O_4$, where V represents cationic vacancies in the lattice, and $y = 0$ is for pure magnetite, while $y = 1$ is for maghemite (γ-Fe_2O_3, fully oxidized magnetite). At temperatures lower than 860 K, the tetrahedral sites in magnetite are occupied by Fe^{3+} ions, while the octahedral sites are populated with Fe^{2+} and Fe^{3+} ions in equal proportions, ensuring a ratio of 2 between Fe^{3+} and Fe^{2+} cations [23]. Substitution with Mg^{2+}, Zn^{2+}, or Al^{3+} cations improves the stability of the ferrites, while transition metals such as Ni^{2+}, Cu^{2+}, Mn^{2+}, or Co^{2+} strongly modify their redox properties [29]. Some ferrites where Fe^{3+} was partly substituted by M^{3+} cations (e.g., Gd^{3+}) [68] showed enhanced electrical properties.

Cobalt ferrite has a cubic spinel structure, with the Co^{2+} ions preferably placed in the octahedral sites, but not exclusively, the distribution reportedly depending on the thermal treatment of the sample [69]. When manganese or chromium ions substitute some of the Fe^{3+} ions, they enter in the octahedral sites and displace some of the Co^{2+} intro tetrahedral sites [69, 70], and chromium is more effective than manganese for this displacement [69]. $NiFe_2O_4$ ferrite has an inverse spinel cubic structure, with the tetrahedral sites completely occupied by Fe^{3+} ions, while the octahedral sites are occupied by Ni^{2+} and Fe^{3+} cations [20, 36, 71]. When zinc replaces some of the Ni cations, a mixed spinel structure, $Ni_{1-x}Zn_xFe_2O_4$, is obtained [72], with Zn^{2+} ions strongly preferring the tetrahedral sites and Ni^{2+} the octahedral ones. The normal spinel structure of $ZnFe_2O_4$ results when all the nickel ions are replaced by Zn. Manganese ferrite has a cubic structure [30] with a partial inverse cation distribution: ca. 20% of the Mn^{2+} cations are situated in octahedral sites, while the rest occupy tetrahedral positions [63]. $CuFe_2O_4$ has a stable, low temperature phase with tetragonal distortion due to the Jahn-Teller effect of the Cu(II) ions, but above 760 °C the structure becomes cubic [64]. When the solid is cooled down slowly to room temperature, the tetragonally distorted spinel structure is observed, while rapid quenching from high temperature maintains the cubic lattice [64]. The tetragonal Cu ferrite is an inverse spinel, with the Cu^{2+} ions sitting mainly in the octahedral sites and the Fe^{3+} found in almost equal proportions in both octahedral and tetrahedral sites [64].

The catalytic properties of ferrites together with the nonstoichiometry and number of vacancies depend significantly on the cation distribution in the tetrahedral or octahedral sites in the spinel structure [7, 38, 73] and on the preparation method [35, 44, 64]. Since the octahedral sites are almost exclusively exposed at the surface, cation species that occupy them are determinant for the catalytic activity [7, 8, 54]. It is believed that the cations occupying tetrahedral sites are inactive or less active

from catalytic point of view due to stronger metal-oxygen bonds and lack of accessibility to reactants [54]. The redox and electronic properties that are of interest in catalysis can be tuned by varying the chemical composition of ferrites, by substituting part of the M^{2+} or Fe^{3+} cations with different cations to obtain mixed ferrites [38, 39, 43, 74].

1.2.1 Preparation Methods

Several methods are mentioned in the literature for the preparation of ferrite nanoparticles, as follows:

- Coprecipitation [5, 6, 28, 35, 36, 44, 45, 47, 60, 64, 74–76], by far the most common route, usually starting from the metal nitrates, but also from chloride [46, 60, 77], acetate [75], sulphate [50, 51], or industrial Cu-rich sludge [78]. NaOH [36], Na_2CO_3 [44], NH_4OH [21, 60, 77], or $H_2C_2O_4$ [60] were used as precipitating agents. Different sizes were reported for the nanoparticles (as small as 2 nm [23], but usually above 20 nm [21, 44, 75]) and with medium to high surface areas. However, impurity phases (e.g., α-Fe_2O_3 [21, 28, 46, 60]) were sometimes reported besides the spinel ferrite phase, possibly due to loss of M^{2+} cation during washing [75]. This method can be used in combination with other techniques, such as sonochemical, high-energy ball milling [23, 44], or combustion [27]. In order to avoid the formation of secondary phases, it was proposed [40, 58, 79] to prepare first a layered double hydroxide precursor with a $M^{2+}/(Fe^{2+} + Fe^{3+})$ molar ratio of 1/2, which, upon calcination, would lead to a pure ferrite phase;
- Citrate precursor [20, 21, 29, 64, 72, 80], with citric acid added usually in excess [49, 70, 81] for the complete coordination of metallic ions, and sometimes followed by self-combustion [8, 49, 70, 72] or freeze drying [81]; from this method, pure ferrite phases were reported [8, 21, 49, 70, 72, 81];
- Solvothermal, mainly using water (hydrothermal) [23, 29, 31, 36, 47, 48, 67, 76, 82], but also organic solvents (ethylene glycol [30], triethylene glycol [22]). The synthesis is conducted in autoclave reactors at temperatures above 100 °C (usually above 200 °C), in some cases in the presence of surfactants (the same as the solvent, but sometimes different, e.g., cetyl trimethyl ammonium bromide, CTAB [31]), and yields high surface area solids [31, 48]. Some authors [82] reported the formation of a Fe_2O_3 side phase besides the ferrite product;
- Sol-gel [7, 29, 36, 37, 59, 66], sometimes followed by self-combustion [34, 39, 83, 84] or supercritical drying [58]. Common fuels in self-combustion are dextrose ($C_6H_8O_7$), glucose ($C_6H_{12}O_6$), sucrose ($C_{12}H_{22}O_{11}$), urea (CH_4N_2O), and glycine ($C_2H_5NO_2$) [84]. Alternatively, self-combustion can be ignited by an electrically heated wire [83]. These fuels form complexes with the metal cations in solution, enabling homogeneous distribution, and generate heat in exothermic process. The solids need to be calcined in a final step to eliminate all traces of organic compounds;

- Solid-state reaction (ceramic technique) [25, 29, 52, 64, 67, 69, 71, 85], starting from the metal oxides that are calcined at high temperatures (usually above 1000 °C). Because of the high temperatures and long thermal treatment times required for the preparation, in some cases phase separation and nonstoichiometry occur [58]. If temperature is not high enough, or time is not sufficiently long, incomplete reactions in the solid state lead to impurity phases (e.g., α-Fe_2O_3), [85];
- Thermal decomposition of polynuclear coordination compounds [6, 32, 43, 61, 86–88], using complexing agents such as tartaric acid [6, 43]. Pure ferrite phases were obtained in many cases [32, 61, 87, 88], but some reports mention the presence of side oxide phases [6];
- Mechanochemical [5], starting from the metal salts (nitrates [5] or chlorides [89]) in stoichiometric ratio. The salts are grounded in a mechanical mortar until they dissolve in their crystallization water, then crystalline ammonium carbonate [5] or sodium borohydride [89] is added. In the case of $(NH_4)_2CO_3$, a paste is formed, then calcined to form the ferrite phase [5], while the use of $NaBH_4$ leads directly to ferrite [89];
- Combustion [23, 24, 27, 43, 55, 63, 90] is used because the heat generated in the exothermic reaction accelerates the process, and it produces nanosized oxide particles [42, 91]. Typically, a concentrated solution of the precursors, such as metal nitrates and urea [42], glycine [63, 91], or glycerol [63], is heated at high temperatures for a short time, so the excess water is evaporated and then ignition occurs to produce the very fast synthesis reactions. Pure ferrite catalysts were obtained using this procedure [42, 63, 91]. The nanoscale crystalline-sized solid obtained by this method was explained [91], taking into consideration two factors: (1) an atomic or molecular dispersion of the reactants before combustion, so when ignition occurs only a short-distance diffusion of atoms is necessary for the nucleation to take place; and (2) the rate of the combustion reaction is so high that there is not enough time for the long-distance diffusion of atoms that would lead to a growth of the crystallites. The characteristics of the obtained solids can be tuned by modifying the intensity of the combustion reaction through the variation of the oxidizer-to-fuel ratio or by mixing different fuels, which determine the combustion reaction temperature [63];
- Water-in-oil microemulsion [21, 92, 93], starting from metal salts (e.g., nitrates) and using an organic solvent (e.g., *n*-octane [92], xylene [93] or heptane [21]), surfactants such as cetyl trimethyl ammonium bromide (CTAB) [92], sodium dodecylbenzenesulfonate (NaDBS) [93], or poly(oxyethylene)nonylphenyl ether [21] for the preparation of the microemulsion, and NH_4OH [21, 92] or hydrazine [93] as precipitating agent. The metal hydroxides precipitate is formed, being confined in the microemulsion droplets. These droplets act as nanosized reactors for the precipitation reaction, since the surfactant layer surrounding them prevents the coagulation of the particles [92]. From this preparation route, pure ferrite phases were reported, with particle sizes below 20 nm [21, 92, 93], the size being controlled by varying the relative concentration of the metal salts, surfactant, and solvent [93].

Ferrites prepared by different methods lead to different physical (e.g., specific surface area) [20, 36, 76] and catalytic properties [36, 76]. For hydrothermal [36, 67, 76], sol-gel [7, 36], and citrate precursor self-combustion [20] methods, single-phase pure ferrite was reported, while solid-state reaction and coprecipitation produced in some cases [36, 67, 76] mixtures of ferrites with the corresponding oxides. For $NiFe_2O_4$ ferrites obtained by coprecipitation, the surface Fe/Ni ratio observed by XPS analysis was very high as compared to theoretical values, confirming the presence of impurity oxides besides the ferrite phase [36, 76]. Also, as the particle size decreases, a change in the ferrite structure is observed, from inverse spinel to mixed spinel [20].

Nanosized spinel ferrites proved to be a viable alternative for combustion catalysts, even for stable and nonreactive molecules [5, 8, 59].

One drawback of the ferrite catalysts is their rather small specific surface area [7, 8, 49, 66, 77, 84]. Some studies used ferrites supported on high surface area supports (e.g., silica [59]) in order to improve dispersion and, therefore, the catalytic activity. Other studies used core-shell multicomponent structures that prevent sintering and aggregates forming at high temperatures [77]: e.g., a $NiFe_2O_4$ core, with a SiO_2 shell porous enough to allow reactants and products transport to and from the catalytic core surface.

1.2.2 Ni–Fe Spinels

Benrabaa et al. [36] observed that in $NiFe_2O_4$ prepared by sol-gel method some of the Ni^{2+} ions were placed in tetrahedral sites, where they are less stable than in octahedral sites. This influences the H_2-TPR behavior of the ferrite, with Ni^{2+} being reduced at lower temperatures, and in turn, influences the catalytic activity of the ferrite [36].

H_2-TPR experiments of $NiFe_2O_4$ prepared by coprecipitation route [45] showed two peaks, one at low temperature (350 °C) attributed to reduction to Ni and Fe_3O_4, the second one at higher temperatures (ca. 520 °C), belonging to the reduction of Fe_3O_4. Magnetite prepared by the same route as the Ni ferrite showed three main reduction events: the low temperature one (400 °C) corresponded to FeO(OH) impurity species being reduced to Fe_3O_4, the second (550 °C) and the third one (650 °C) significantly overlapping were attributed to the reduction of magnetite to FeO and Fe. By comparing the reduction profiles of the two ferritic materials, it has been concluded that the presence of Ni^{2+} ions increases the reducibility of magnetite. This feature has a positive effect on the catalytic activity of ferrites when lattice oxygen is involved in oxidation reactions.

Nickel, cobalt, and magnesium ferrites were prepared from layered double hydroxides as precursors, and then coated with SiO_2 and Al_2O_3 to be used in applications as catalysts or catalyst supports [79]. The layered double hydroxides precursors were prepared by coprecipitation from nitrates, using NaOH and Na_2CO_3 as precipitating agents. By calcination at 900 °C, pure spinel ferrites were obtained,

which were covered with a SiO_2 coating (1–3 μm) by using a Na_2SiO_3 solution. The final porous Al_2O_3 coating was deposited from an alumina sol using hexamethylenetetramine solution as coagulating agent, the final solid having a ferrite/SiO_2/Al_2O_3 mass ratio of 7.6/7.3/85.1. Since the silica and alumina shells are porous (average pore size ca. 20 nm) and have high specific surface areas (ca. 190 $m^2\ g^{-1}$), the final solid can be used as catalyst or catalyst support and can also be magnetically recovered from the reaction due to the ferrite core.

A $NiFe_2O_4$@SiO_2 core-shell structure was prepared [77] in a one-pot synthesis, starting from $FeCl_2$, $Ni(NO_3)_2$ and NH_4OH, in the presence of a surfactant (polyethylene glycol hexadecyl ether dissolved in cyclohexane). After the ferrite was precipitated, a tetraethyl orthosilicate solution in methanol was added to provide the shell. It has been observed that the concentration of surfactant determined the shape of the final nanoparticles: nanorods were obtained instead of nanospheres when the concentration was doubled. Nickel ferrite nanoparticles with inverse spinel structure were prepared at 500 °C, with a secondary impurity phase of amorphous Ni oxide, but at 900 °C a Fe_2O_3 phase was also observed. The H_2-TPR profile for the uncoated $NiFe_2O_4$ shows that the reduction at low temperatures leads to the formation of metallic Ni + Fe_2O_3. The SiO_2 coating stabilized the ferrite and delayed the reduction until higher temperatures. It was proposed that the Fe_2O_3 phase formed by aggressive reduction of the core-shell structure may segregate to the surface and delay reduction of the underlying species. The porous shell allows transport to and from the core surface, but also prevents or retards sintering of the core particles, which can be used as catalysts over a large range of temperatures.

1.2.3 Co–Fe Spinels

The structural and chemical evolution of a $CoFe_2O_4$ spinel, prepared by solid-state reaction, was investigated by in situ neutron diffraction in isothermal conditions (900 °C) when the partial pressure of oxygen was lowered from $10^{-0.9}$ to 10^{-19} atm [85]. The composition of the solid was determined to be CoO $n$$Fe_2O_3$ (n = 1 and 2), in two phases: a $Co_{0.27}Fe_{0.73}(Co_{0.35}Fe_{0.65})O_4$ spinel, and a second phase containing a mixture of the spinel with unreacted α-Fe_2O_3. The spinel (content of the octahedral sites shown in brackets) had a composition with a slightly higher inversion degree, but close to the stoichiometric ferrite (Co:Fe = 1:2), and the second phase contained 64 wt. % spinel (with identical composition as the first phase) and 36 wt. % hematite. As the partial pressure of oxygen decreased (corresponding to a reduction reaction), the evolution observed for the second phase was: α-Fe_2O_3 → (Fe, Co)$_3O_4$ spinel → (Fe, Co)$_{1-x}$O wustite → (Fe, Co)O rock salt → γ-(Fe, Co) alloy → α-(Fe, Co) alloy. In the first step of the reduction, hematite is converted to magnetite with a spinel structure:

$$6Fe_2O_3\,(\text{hematite}) \rightarrow 4Fe_3O_4\,(\text{magnetite}) + O_2 \tag{1.1}$$

From diffraction patterns during reduction, it was proposed that the transformation involved a homogeneous internal process, in which the Fe spinel spontaneously precipitated at the interface between hematite and the Co spinel from adjacent grains.

$CoFe_2O_4$ was prepared by Tong et al. [34] by a self-combustion method starting from nitrates and citric acid, with different molar ratios between Co^{2+} and Fe^{3+}, i.e., 1:4.0; 1:2.8; 1:2.0; 1:1.5; and 1:1.1. The purpose of the study was to prepare nonstoichiometric spinel ferrites. Pure spinel cobalt ferrite was obtained only for the stoichiometric ratio (1:2.0). The other solids did not contain nonstoichiometric ferrites, but just either Fe_2O_3 (first two samples) or Co_2O_3 (the last two samples) additional phases. The mean particle sizes, determined from the XRD pattern, decreased from 34 to 21 nm as the Co:Fe molar ratio decreased.

The same self-combustion route was used by Bhagwat et al. [84] to prepare $CoFe_2O_4$, starting from the metal nitrates and using different fuels for the combustion step: ethylene glycol, glycine, and urea. All obtained solids were pure ferrites, without impurity phases and had similar sponge-like morphologies. The crystallite size (calculated from the XRD patterns) and specific surface areas were influenced by the organic compound used as fuel: the smallest particles (~15 nm) were obtained with urea, while glycine yielded the largest crystallites (~22 nm). The differences were attributed to the different ignition temperature and heat of combustion generated by the fuels.

A different study investigated the Ni and Co ferrites prepared by the citrate method [81] using four different procedures: (1) the metal citrate precursor solutions (0.3 M metal salt solution, metal-to-citric acid ratio = 1:1, 10% excess citrate, pH = 7) were freezed at −80 °C, then sublimated at −48 °C and l50 mTorr for 48 h; (2) the same procedure, but with metal-to-citric acid ratio = 1:2; (3) the same procedure as in (1), but with pH = 10; (4) the same procedure as in (1), but with diluted metal salt solutions (0.15 M). The FT-IR study of the precursors showed that, as the ratio between metal and citric acid increased, the bands attributed to citric acid are progressively replaced with those belonging to deprotonated citrate groups, while those related to hydrogen bonding in citric acid molecule are substituted by a diffuse band corresponding to a protonated hydroxyl group. These findings led the authors to conclude that a triionized citrate ligand was chelating the transition metal ions. The XRD patterns showed the formation of highly crystalline ferrites, while in the case of the sample obtained with metal-to-citric acid ratio = 2, a small diffraction line corresponding to hematite impurity was observed. The preparation procedure had a marked effect on the morphology of the solids: bulky particles resulting by the aggregation of primary particles were observed when the amount of citric acid was doubled, while at higher pH a corrugated web of microfibers was obtained. As the calcination temperature was increased from 600 to 1000 °C, increased crystallinity and crystallite sizes were observed due to sintering.

The synthesis of $CoFe_2O_4$ was investigated by Yan [91] using three routes: combustion, sol-gel, and solid-state reaction, the resulted solids having similar characteristics. In the combustion method, glycine, serving as a fuel for the combustion reaction, was oxidized by the nitrate ions. In order to completely decompose the residual organic compounds, the solids were calcined afterwards. By modifying the

glycine-to-nitrate (*G*/*N*) ratio, the reaction temperature can be controlled and, consequently, the crystallite size of the obtained ferrite. The authors observed that, for *G*/*N* values in the investigated range (0.2–2.5), the lower the *G*/*N* ratio, the smaller the sizes for the ferrite crystallites.

$CoFe_2O_4$ and $MgFe_2O_4$ were studied as catalysts for the total oxidation of methane, together with several Cr-based spinels prepared by solution combustion route [42]. The synthesis method was adopted for the pure spinels that it produces, with relatively high specific surface areas compared to other methods. T_{50} (temperature corresponding to 50% CH_4 conversion) was used as an index for the catalytic activity. The two ferrite catalysts showed poor results (T_{50} of 549 °C and 580 °C, respectively) and total conversion at ca. 620 °C, while the Cr-based spinels had higher activity (T_{50} of 369 °C and total conversion below 500 °C, similar to Pd/γ-Al_2O_3), mainly due to their higher specific surface areas. The authors observed a strong correlation between the catalytic activity and the oxygen desorption capacity, namely the amount of α oxygen desorbed at low temperature (below 450 °C), where the most active spinels displayed their combustion activity [42].

Methane combustion was also investigated on Co ferrites obtained by thermal decomposition of ferrioxalate coordination compounds [61]. The oxalate precursor was prepared in situ from 1,2-ethanediol and nitric acid (1 M or 2 M), with Fe and Co nitrates, in aqueous medium. When HNO_3 1 M was used, a $[Fe_2Co(C_2O_4)_3(OH)_2(OH_2)_4]\cdot 2H_2O$ (I) coordination compound was obtained, while $[Fe_2Co(C_2O_4)_4(OH_2)_6]$ (II) compound was synthesized when HNO_3 2 M was used. The corresponding pure ferrites, $CoFe_2O_4$ (I) and $CoFe_2O_4$ (II), were obtained by thermal decomposition of the coordination compounds precursors. Both solids showed mesoporous structures, with nanosized particles (below 12 nm). When tested in the combustion of methane, they displayed good catalytic activities, with $CoFe_2O_4$ (I) showing conversion values only slightly lower than a Pt/Al_2O_3 reference catalyst (Engelhard), but better than $CoFe_2O_4$ (II). However, in stability tests the $CoFe_2O_4$ (I) solid lost about 40% of its activity in the first 3 h on stream. The authors attributed this decline to a collapse of the pore structure and proposed to disperse the high surface area ferrites on thermally stable supports such as barium hexaaluminate [61].

The influence of the preparation method for $NiFe_2O_4$ and $CoFe_2O_4$ was investigated by Urda et al. [5], the prepared ferrites being tested in the combustion of propane. Nickel ferrite was prepared by coprecipitation (method M1) from nitrates using NaOH, while $CoFe_2O_4$ was synthesized, besides the M1 method, by the mechanochemical method (M2) using Co and Fe nitrates and crystalline ammonium carbonate. All solids had cubic spinel structures with, for $CoFe_2O_4$ samples, a small amount of α-Fe_2O_3 side phase. The sample prepared by the M2 method showed higher crystallinity and lower specific surface area. $CoFe_2O_4$-M1 was the most active, leading to complete conversion of propane into CO_2 and H_2O at 400 °C, the order of activity being as follows: $CoFe_2O_4$-M1 > $NiFe_2O_4$-M1 > $CoFe_2O_4$-M2 (Fig. 1.1). $CoFe_2O_4$ prepared by both M1 and M2 methods were stable for 24 h on stream, and their physico-structural characteristics remained unchanged after the catalytic tests [5].

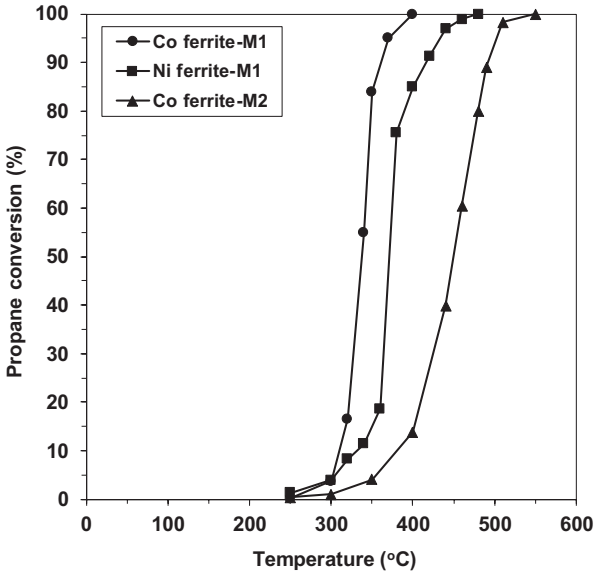

Fig. 1.1 Propane conversion as a function of the reaction temperature for the Co and Ni ferrospinel samples (Reaction conditions: 2% vol. propane in air, total VHSV = 6000 h^{-1}). (Reproduced from ref. [5] with permission)

Pure cobalt ferrite, prepared by pulsed spray evaporation chemical vapor deposition (PSE-CVD) from metal acetylacetonates, was used as catalyst for the low temperature combustion of olefins and dimethyl ether [65]. $CoFe_2O_4$ proved to have high activity for the combustion of propene, 1-butene, and dimethyl ether, without producing CO or hydrocarbon secondary products. This was attributed to the high mobility of oxygen species in the ferrite lattice.

To find correlations between the synthesis procedure and the catalytic activity, $CoFe_2O_4$ was prepared by different coprecipitation procedures and studied in the total oxidation of ethanol [60]. Metal chlorides or nitrates were used as starting materials, and precipitation was achieved with NaOH, NH_4OH, or $H_2C_2O_4$. When NaOH was used as precipitating agent, the formation of spinel structure was observed even before the calcination step, as also observed by Cheng et al. [82], and a pure ferrite phase was obtained after the thermal treatment. A pure ferrite phase was also observed for the samples precipitated with oxalic acid, the spinel phase being formed at temperatures as low as 500 °C. When ammonia was used as precipitating agent, a small amount of Fe_2O_3 side phase was obtained, the sample had smaller specific surface area and, consequently, lower catalytic activity in ethanol oxidation. Solids prepared from chloride salts also showed poor performances, attributed to the poisoning effect of chloride ions. The best results (total conversion at 310 °C) were obtained starting from nitrate salts, using NaOH as precipitating agent and a calcination temperature of 500 °C.

1.2.4 Cu–Fe Spinels

A similar, very detailed study for the influence of the preparation method on the catalytic activity in propane combustion was performed for $CuFe_2O_4$ [64]. The copper ferrite was prepared by three different ways: solid-phase reaction (SP) starting from CuO and Fe_2O_3, coprecipitation from nitrate precursors (NIT), and decomposition of the citric acid precursor (CIT). As expected, the obtained materials had different activities in the catalytic combustion of propane, strongly influenced by the crystal size, cation distribution in the spinel structure, and physicochemical properties (specific surface area, porosity, reducibility) derived from the different preparation procedures. The wet chemical methods (NIT, CIT) produce a spinel structure at lower temperatures than the solid-state reaction, with higher homogeneity and smaller particle sizes. The authors inferred that the presence of Cu ions, both in the octahedral and tetrahedral sites in the structure, keeps the active sites separated, maintaining the stability of the ferrite catalysts. The XRD pattern for the catalyst prepared by SP route showed the formation of ferrite lattice only above 800 °C, and after calcination at 900 °C, displayed the single-phase cubic structure. The samples obtained by the wet chemical methods, which were calcined at 700 °C, showed the tetragonal structure. For the CIT route, a very thorough study of the transformations occurring with increasing calcination temperature was performed using XRD, IR, and TG-DTA techniques. The XRD pattern of a poorly crystallized tetragonal $CuFe_2O_4$ lattice was visible even at 150 °C, and the diffraction lines became more intense with increasing calcination temperature. IR spectra also showed the disappearance of most of the lines attributed to the citrate precursor and the presence of bands belonging to copper ferrite at 150 °C. The TG curve showed a smooth weight loss below 150 °C, attributed to water vaporization, followed by a gradual mass loss between 150 and 300 °C, corresponding to the thermal decomposition of the citrate precursor. Above 300 °C, only a slight mass loss and no thermal effects are observed in the formed ferrite phase. The particle size of the ferrite obtained by CIT route was smaller compared to the ferrites obtained by other methods. The Mössbauer spectra confirmed the presence of Fe^{3+} cation both in the octahedral and tetrahedral sites with almost equal proportions, but in the ferrite from the CIT route the octahedral presence has a slight predominance. EDX scanning of the ferrite obtained from citrate precursor confirmed that Cu and Fe are well-dispersed on the surface of the solid, with Fe/Cu ratio of 2. Consequently, the authors concluded that the ferrites have inverse spinel structures, the degree of inversion depending on the preparation method and calcination temperature. The preparation method had a significant influence on the catalytic activity in propane combustion, the conversion values decreasing in the order: NIT > CIT > SP. It was observed that the presence of Fe^{3+} ions in equal proportions in the typically inverted $CuFe_2O_4$ spinel obtained by the NIT method favored the catalytic combustion of propane compared to the partially inverted spinel obtained by CIT route. Total conversion was obtained for the NIT sample at ca. 650 °C.

Tu et al. [78] investigated the preparation of $CuFe_2O_4$ ferrite from industrial Cu-rich waste sludge and tested it in the catalytic combustion of isopropyl alcohol. The authors studied the influence of reaction temperature (30–500 °C), oxygen content in the reaction mixture (10%, 15%, and 21%), space velocity (GHSV = 8000–30,000 h^{-1}), and alcohol inlet concentration (500–2000 ppm). The best results were obtained at 180 °C, GHSV = 30,000 h^{-1}, oxygen concentration 21%, and 2000 ppm alcohol in the reaction mixture. The catalyst could be recycled five times without any treatment, while stability tests for 100 h showed only a minor decline in the catalytic conversion during the first 24 h on stream, then reaching stable values.

The catalytic combustion of toluene was also investigated on copper ferrites obtained from the respective nitrates by coprecipitation with Na_2CO_3 solution at pH = 9 [35]. The influence of the annealing temperature was investigated between 300 and 800 °C. Below 500 °C, only amorphous materials were obtained, while at higher temperatures the product was a mixture of cubic and tetragonal ferrites, the latter increasing in importance with the annealing temperature. The distortion of the cubic structure with increasing temperature to form the tetragonal phase was attributed to the higher proportion of Cu in octahedral positions. From Mössbauer spectra of the solids annealed below 500 °C, the presence of finely dispersed iron containing particles with sizes below 10–12 nm was noticed. At higher temperatures, the spectra showed the typical octahedral and tetrahedral coordination of Fe^{3+} ions in ferrites and also the presence of Fe^{3+} in a hematite side phase. In the catalytic tests, the higher the annealing temperature, the lower the catalytic activity, an effect that was attributed to the transformation of cubic spinel to the tetragonal one and also to the increase in particle sizes with the annealing temperature. Under reaction conditions, no significant phase change was observed, only further crystallization. The authors observed a good correlation between the activity and the reduction ability determined from H_2-TPR measurements.

1.2.5 Zn–Fe Spinels

The influence of the pH during the synthesis of Zn ferrite by coprecipitation was studied by Lee et al. [46]. The authors used aqueous buffer solutions as coprecipitation medium in order to control the pH and prepared several $ZnFe_2O_4$ samples at pH values between 6 and 12. All preparations produced the desired pure ferrite phase, except for that performed at pH = 6, which also gave α-Fe_2O_3 side phase. The experimental Fe/Zn ratio was in good agreement with the theoretical value, except for the sample prepared at pH = 6 for which it is 3.24, likely due to the formation of Fe_2O_3 phase.

$MeFe_2O_4$ spinels (Me = Zn, Mn, Ni, Co, Cu) were investigated as potential oxygen carriers or reactive support in Chemical Looping Combustion (CLC) of methane [62]. In CLC, direct contact between fuel and air is avoided by using oxygen carriers (such as metal oxides) to transport oxygen from air to the fuel. Combustion

takes place in one reactor, where fuel is oxidized by the oxygen carrier, and the reduced carrier is reoxidized with air in a different reactor. The advantage is that the effluent of the combustion reactor consists only of CO_2 and H_2O; therefore, pure CO_2 can be obtained after steam condensation, without being diluted with N_2. The oxygen carrier must have high oxygen transfer capacity, ferrites being considered good candidates for this process. The pure spinel ferrites were obtained by solid-state reaction at different temperatures (1000 °C for Me = Ni, Zn, and Co; 1165 °C for Mn and 750 °C for Cu), based on the phase diagrams of the corresponding ferrites. Since the CLC process requires redox cycles, the solids were tested to determine their oxygen transfer capacity and the stability during repeated cycles. In this respect, $ZnFe_2O_4$ and $NiFe_2O_4$ showed that they can deliver larger amounts of lattice oxygen compared to $MnFe_2O_4$, but they do not regain all of it during reoxidation; e.g., Ni ferrite is very active during the first cycle (80% CH_4 conversion at 1000 °C), but deactivates very fast (38% conversion in the second cycle) due to sintering and loss of active surface area. $ZnFe_2O_4$ loses activity due to an almost complete decomposition to hematite and metallic Zn. Co and Cu ferrites regain most of the transferred oxygen and are more stable, $CuFe_2O_4$ showing the best performance, with high methane conversions (>99%) and low CO selectivity (max. 6%), although some decomposition to $CuFeO_2$ was also observed in this case. Therefore, the authors concluded that these ferrites can be used either as oxygen carriers (Cu ferrite) or reactive supports for other oxygen carriers (the rest of the ferrites) in the CLC of methane [62].

1.2.6 Mn–Fe Spinels

C_1-C_4 light alkanes were used as test molecules to investigate the catalytic activity of $MnFe_2O_4$ obtained by solution combustion method [63]. It was suggested that the existence of manganese ions in various oxidation states (Mn^{2+} and Mn^{3+} were detected by XPS) could be useful in redox catalytic reactions. The fuel for the combustion consisted of a mixture of glycerol and glycine in various proportions, i.e., 1:0, 0.75:0.25, 0.5:0.5, and 0.25:0.75, and after ignition, the obtained solid was thermally treated in argon flow at 400 °C. Single-phase ferrites were obtained in all cases, with crystallite sizes increasing with glycine proportion in the fuel (from ca. 8 to 73 nm), due to the fact that combustion proceeds very rapidly and a higher amount of heat is released by glycine. The solids obtained with fuel mixtures containing up to 50% glycine showed similar textural and catalytic properties, while the ferrite obtained with 75% glycine had different properties, such as lower specific surface area, larger pores, different morphology (polyhedron shape, compared to spherical for the other three solids), different surface Mn/Fe atomic ratio, different reduction behavior, and lower catalytic activity. The temperature corresponding to 50% conversion decreased from C_1 to C_4 (450 °C for methane, 300 °C for ethane, 240 °C for propane, and 225 °C for butane), but, for each tested compound, the

observed values were identical or very close for the ferrites prepared with up to 50% glycine.

1.2.7 Ternary and Quaternary Ferrites

$Ni_{0.5}Co_{0.5}Fe_2O_4$, $CuFe_2O_4$, and $MgFe_2O_4$ were tested by Rezlescu et al. [66] in the catalytic combustion of acetone. The ferrites, prepared by sol-gel self-combustion route starting from nitrate salts, had spinel structures without impurity phases: Mg- and Ni/Co samples showed cubic spinel structures, while Cu-ferrite had a tetragonal distorted lattice due to Cu^{2+} ions. They showed a rather poor activity in the catalytic combustion of acetone, none of them exhibiting complete conversion up to 550 °C. Cu ferrite, with ca. 95% acetone conversion at 550 °C, showed the best activity. The authors concluded that the higher activity observed for the Cu- and Ni/Co samples is due to the variable oxidation state of the Cu, Ni, and Co ions distributed in the octahedral sites of the spinels.

$Ni_{0.5}Co_{0.5}Sc_xFe_{2-x}O_4$ (x = 0.05; 0.1 and 0.2) [7] and $MgFe_2O_4$ [83] ferrites, prepared by a sol-gel self-combustion method starting from metal nitrates, polyvinyl alcohol, and NH_4OH, were tested in the catalytic combustion of acetone, propane, and benzene. In $Ni_{0.5}Co_{0.5}Sc_xFe_{2-x}O_4$, only low amounts of iron can be replaced by scandium, due to the large difference between their ionic radii (0.069 nm for Fe vs. 0.088 nm for Sc). An inverse spinel structure was observed for all samples, in which the Sc^{3+} ions preferred the octahedral coordination. With scandium incorporation, the crystallite size decreased while the specific surface area increased, attributed to the structural disorder produced by the voluminous Sc ions leading to a delay in crystallite growth. The catalytic tests showed a temperature shift towards lower values upon scandium incorporation, the activity increasing substantially with Sc loading. The best results were obtained for the solid with x = 0.2, and for propane and acetone, without deactivation for 40 h on stream. These results were attributed to the smaller crystallite size, larger surface area, and the presence of oxygen vacancies in the ferrite structure due to scandium ions present in the octahedral sites [7]. Similar results were obtained for $MgFe_2O_4$ in the combustion of propane, acetone, and benzene [83] and of Pb-free gasoline vapors [90].

A similar study was conducted for $Ni_{0.5}Co_{0.5}Sc_xFe_{2-x}O_4$ ferrites (x = 0.1 and 0.2), prepared by the same citrate route followed by self-combustion [8]. Their activity was compared with that of some perovskites with related compositions, in the catalytic combustion of propane. The authors observed the same preference of Sc^{3+} ions for the octahedral site in the ferrite structure, but they observed a decrease in propane conversion as scandium loading increased, contrary to the findings of Rezlescu et al. [7].

Total oxidation of toluene was investigated on several nickel and manganese ferrite catalysts obtained by two different methods: (1) hydrothermal synthesis and (2) ceramic method involving oxides calcination [67]. Cubic spinel $Ni_{0.5}Fe_{2.5}O_4$ and $Mn_{0.65}Fe_{2.35}O_4$ ferrites were obtained by hydrothermal synthesis procedure. $NiFe_2O_4$,

$Ni_{0.5}Zn_{0.5}Fe_2O_4$, and $MnFe_2O_4$ were intended to be prepared by the ceramic method, but incomplete ferritization was observed, leading to a complex mixture of phases. For the first two samples, NiO and ZnO, respectively, were observed in different amounts, besides the ferritic phase, while the last sample consisted of a mixture of α-Fe_2O_3 and Mn_2O_3. The well-structured, pure ferrites obtained hydrothermally showed a very low catalytic activity in the total oxidation of toluene, while the mixture of α-Fe_2O_3 and Mn_2O_3 was the most active catalyst, with conversion values over 80% at 500 °C. The authors presumed an intrinsic, intimate interaction between the individual oxidic phases, since a test performed in similar conditions on a physical mixture of the two oxides, or of the ferrites with the corresponding oxides, showed poor catalytic activity.

Carp et al. [86] explained the differences resulted in the structure and properties of the Ni-substituted Zn ferrites obtained by several preparation methods. There are two problems that have to be overcome when preparing modified zinc ferrites: (1) zinc is volatile at high temperatures, changing the stoichiometry of the final product and also leading to Fe^{2+} formation, and (2) the presence of three different cations, possibly resulting in different intermediate and final phases. When solid-state reaction is used for the preparation, a mixture of simple ferrites is formed instead of $Zn_{1-x}Ni_xFe_2O_4$, while a homogeneous ferrite is obtained only above 750 °C. The hydrothermal route produces either individual ferrites or defective, nonstoichiometric oxides, and the real stoichiometric ferrites are formed at 850 °C. The combustion method leads to a pure Ni-Zn ferrite at 1100 °C, but the decomposition of a polynuclear coordination compound (with the malate anion as ligand) produced the mixed $Zn_{1-x}Ni_xFe_2O_4$ ferrite (prepared with $x = 0.25$, 0.50, and 0.75) at relatively low temperature, i.e., 500 °C, while evolving nontoxic compounds (CO_2 and H_2O). IR spectra suggested that the malic acid ($C_4H_6O_5$) is coordinated to the metal ions both through its two carboxyl groups and its OH group. The final ferrites were obtained with crystallite sizes in the range of 65–85 nm.

$ZnFe_{2-x}Nd_xO_4$ ($x = 0$; 0.25; 0.5; 0.75; and 1) were prepared by Papa et al. [43] using the combustion route from tartrate precursors and then tested in the catalytic combustion of methane. As the Fe^{3+} ions are progressively replaced by Nd^{3+}, the cubic structure of the zinc ferrite coexists with the newly formed orthorhombic phase of $NdFeO_3$. The authors explained the formation of the latter phase by a limited solubility of Nd^{3+} ions with larger ionic radius (1.16 Å compared to 0.87 Å for Fe^{3+}) in the spinel lattice. The $ZnNd_2O_4$ oxide showed a distorted tetragonal structure, with $(ZnO_2)^{2-}$ and $(Nd_2O_2)^{2+}$ alternating units, in which Nd^{3+} are surrounded by $8O^{2-}$ ions, while Zn^{2+} only by $4O^{2-}$ ions. The catalytic activity in methane combustion showed a maximum (in the kinetic regime) at $x = 0.5$, where the authors postulated the highest concentration of lattice defects. Since Fe^{3+} and Nd^{3+} have the same oxidation state, these defects are not electrically charged, but due to significant differences in their ionic radii, lattice strains appear and a new crystalline phase is formed. In this way, the reduction behavior changes and the oxygen mobility within the lattice is affected. The catalytic combustion activity is therefore related to the degree of Fe^{3+} substitution with Nd^{3+} in the octahedral positions of the spinel.

$Cu_xCe_{1-x}Fe_2O_4$ ferrites (x = 0; 0.2; 0.5; 08; 1) prepared by a sol-gel method followed by self-combustion were also studied as catalysts in toluene combustion [39]. The XRD patterns showed the inverse spinel structure gradually disappearing as Ce loading increased, while CeO_2 diffraction lines were observed starting from $x = 0.8$. A decrease in the pore sizes was observed with increasing Ce content, while the BET surface areas remained constant and low (10 $m^2\ g^{-1}$). The catalytic activity decreased in the order: $Cu_{0.8}Ce_{0.2}Fe_2O_4 > Cu_{0.5}Ce_{0.5}Fe_2O_4 > CuFe_2O_4 > Cu_{0.2}Ce_{0.8}Fe_2O_4 > CeFe_2O_4$. The authors found a correlation between the order of activity and the amount of surface electrophilic oxygen and oxygen vacancies, with a maximum concentration at $x = 0.8$. At the same x value, the XPS measurements showed a maximum for the Ce^{3+}/Ce^{4+} ratio that decreased at higher Ce content. This suggested that the presence of Ce^{3+} facilitates the formation of oxygen vacancies and promotes the catalytic activity in toluene combustion.

The different ferrospinel catalysts hereby described are summarized in Table 1.1 together with their preparation methods and catalytic applications in VOC combustion.

1.2.8 The Redox Properties of Ferrites

The reducibility of ferrites can be modified by incorporation of different M^{2+} cations in the spinel structure and, in turn, it significantly influences the catalytic activity due to altered redox properties [73]. Khan and Smirniotis studied the H_2-TPR profiles of some MFe_2O_4 spinels (M = Cr, Mn, Co, Ni, Cu, Zn, and Ce) obtained by coprecipitation and compared them with the individual oxides. The authors observed that the positions of the temperature maxima were strongly influenced by the nature of the cation: Cu^{2+} showed the strongest shift of the $Fe_2O_3 \rightarrow Fe_3O_4$ reduction peak with ca. 160 °C to lower temperatures, followed by Mn^{2+} (50 °C) > Ce (ca. 40 °C) > Ni ≈ Co (30 °C) > Cr ≈ Zn (no shift). However, the maximum for the reduction of Fe_3O_4 to FeO was less influenced, while the FeO → Fe reduction peak was not shifted. These features can be correlated with the catalytic activity when redox reactions are involved [73].

Electrical conductivity measurements of spinel ferrites allowed to find correlations between their semiconductive and redox properties and their catalytic activity in oxidation reactions. Mathe and Kamble [75] studied $Ni_{0.4}Co_{0.6}Fe_2O_4$ ferrite and observed five domains with different slopes in the plot of $\ln(\rho)$ versus $1/T$, in the temperature range 300–900 K (where ρ represents the electrical resistivity). Besides the usual domains attributed to conduction by impurities, ferromagnetic and paramagnetic conduction, the authors identified a temperature interval (500–833 K) where some of the Fe^{3+} ions in the spinel lattice slowly migrate from tetrahedral to octahedral sites. This alteration of the cation distribution between the two types of sites will not lead to a modified crystal structure, but will affect the electrical conductivity of the solid.

Table 1.1 Preparation and catalytic performance of the ferrospinel catalysts in VOC total oxidation

Catalyst	Preparation method	Tested chemical compound (reaction conditions)	Best results	Ref.
Co ferrite and Mg ferrite	SolC[a] synthesis	Methane (200–750 °C, 2.5 or 0.4% CH_4/7.5% O_2/He balance; W/F = 0.12 g s cm^{-3})	$T_{100} \approx 620$ °C on Co ferrite	[42]
Co ferrite	TD[b] of ferrioxalate coordination compounds	Methane (300–650 °C, 100 cm^3 min^{-1} (60,000 mL g^{-1} h^{-1}), 1 vol. % CH_4, 10% O_2, Ar balance)	$T_{100} = 600$ °C	[61]
$ZnFe_{2-x}Nd_xO_4$ ($x = 0$; 0.25; 0.5; 0.75; 1)	TD[b] of polynuclear coordination compounds	Methane (400–700 °C, GHSV = 60,000 h^{-1}, 2% CH_4, 10% O_2, Ar balance)	$T_{100} \approx 675$ °C on $ZnFe_{2-x}Nd_xO_4$ with $x = 0.25$ and 0.5	[43]
$CuFe_{2-x}Mn_xO_4$ ($x = 0$; 0.4; 0.8; 1.6; 2)	SSR[c]	Methane (500–770 °C, GHSV = 15,000 h^{-1}, 1% CH_4 in air)	Conversion of ca. 65% at 770 °C on Cu ferrite ($x = 0$)	[38]
Mn ferrite	SolC[a]	Methane (GHSV = 60,000 h^{-1}, 0.01% CH_4, 20% O_2, N_2 balance)	$T_{50} = 450$ °C	[63]
Me ferrite (Me = Mn, Ni, Zn, Co, Cu)	SSR[c]	Methane (chemical looping combustion at 1000 °C, in a pulse reactor)	Conversion > 99% for Cu ferrite	[60]
Mn ferrite	SolC[a]	Ethane (GHSV = 60,000 h^{-1}, 0.01% C_2H_6, 20% O_2, N_2 balance)	$T_{50} = 300$ °C	[63]
Ni ferrite, Co ferrite	CoPP[d] and mechanochemical methods	Propane (250–600 °C, VHSV = 6000–11,000 h^{-1}, 2% propane in air)	$T_{100} = 400$ °C for CoPP Co ferrite at 6000 h^{-1}	[5]
$Ni_{0.5}Co_{0.5}Sc_xFe_{2-x}O_4$ ($x = 0.05$; 0.1 and 0.2)	SG[e] + SelfC[f]	Propane (50–550 °C, GHSV = 5100 h^{-1}, 1–2‰ C_3H_8 in air)	Conversion of ca. 92% at 500 °C	[7]
$Ni_{0.5}Co_{0.5}Sc_xFe_{2-x}O_4$ ($x = 0.05$; 0.1 and 0.2)	SG[e] + SelfC[f]	Propane (50–500 °C, GHSV = 5100 h^{-1}, 1–2‰ C_3H_8 in air)	$T_{90} \approx 370$ °C on $Ni_{0.5}Co_{0.5}Fe_2O_4$	[8]

(continued)

Table 1.1 (continued)

Catalyst	Preparation method	Tested chemical compound (reaction conditions)	Best results	Ref.
Cu ferrite	SSR[c], CoPP[d], and CitP[g]	Propane (200–750 °C)	T_{100} = 650 °C for the ferrites prepared by CoPP and CitP	[64]
Cu ferrite	CoPP[d]; TD[b] of polynuclear coordination compounds	Propane (25–450 °C, C_3H_8:O_2 = 1:0.9–1:6 (mol/mol), contact time = 1 and 2 s)	T_{100} = 390 °C for the sample obtained by TD	[6]
Mg ferrite	SG[e] + SelfC[f]	Propane (20–550 °C, GHSV = 5100 h^{-1})	T_{50} = 312 °C	[83]
Mn ferrite	SolC[a]	Propane (GHSV = 60,000 h^{-1}, 0.01% C_3H_8, 20% O_2, N_2 balance)	T_{50} = 240 °C	[63]
Mn ferrite	SolC[a]	Butane (GHSV = 60,000 h^{-1}, 0.01% C_4H_{10}, 20% O_2, N_2 balance)	T_{50} = 225 °C	[63]
Co ferrite	PSE-CVD[h]	Propene (220–460 °C, WHSV = 45,000 mL g_{cat}^{-1} h^{-1}, 1% propene, 10% O_2, Ar balance)	T_{50} = 348 °C T_{90} = 382 °C	[65]
Co ferrite	PSE-CVD[h]	1-butene (220–460 °C, WHSV = 45,000 mL g_{cat}^{-1} h^{-1}, 1% butene, 10% O_2, Ar balance)	T_{50} = 358 °C T_{90} = 402 °C	[65]
$Ni_{0.5}Fe_{2.5}O_4$ $Mn_{0.65}Fe_{2.35}O_4$ Ni ferrite $Ni_{0.5}Zn_{0.5}Fe_2O_4$	HT[i], SSR[c]	Toluene (150–500 °C, GHSV = 60,000 mL g_{cat}^{-1} h^{-1}, 1700 ppm toluene)	Conversion of ca. 80% at 500 °C on $MnFe_2O_4$	[67]
Cu ferrite	CoPP[d] and calcination at different temperatures	Toluene ($p_{toluene}$ = 0.9 kPa, WHSV = 1.2 h^{-1})	T_{100} = 325 °C on the sample annealed at 300 °C	[35]
$Cu_xCe_{1-x}Fe_2O_4$ (x = 0; 0.2; 0.5; 0.8; 1)	SG[e] + SelfC[f]	Toluene (100–300 °C, 300 mg m^{-3} toluene in air, $p_{toluene}$ = 0.8 MPa, GHSV = 6000 h^{-1})	T_{90} = 215 °C for $Cu_{0.8}Ce_{0.2}Fe_2O_4$	[39]

(continued)

Table 1.1 (continued)

Catalyst	Preparation method	Tested chemical compound (reaction conditions)	Best results	Ref.
Co ferrite	CoPP[d]	Ethanol (200–400 °C, GHSV = 30 m^3 h^{-1} kg^{-1})	T_{100} = 310 °C on $CoFe_2O_4$ prepared from nitrates, precipitated with NaOH and calcined at 500 °C	[60]
Cu ferrite	CoPP[d]	Isopropyl alcohol (30–500 °C, GHSV = 8000–30,000 h^{-1}, 500–2000 ppm alcohol, 10–21% O_2)	T_{100} = 180 °C, GHSV = 30,000 h^{-1}, 21% O_2, 2000 ppm alcohol	[78]
Cu ferrite, Mg ferrite, $Ni_{0.5}Co_{0.5}Fe_2O_4$	SG[e] + SelfC[f]	Acetone (50–550 °C, GHSV = 5100 h^{-1}, 1–2‰ in air)	Conversion of ca. 95% at 550 °C on Cu ferrite	[66]
$Ni_{0.5}Co_{0.5}Sc_xFe_{2-x}O_4$ (x = 0.05; 0.1 and 0.2)	SG[e] + SelfC[f]	Acetone (50–550 °C, GHSV = 5100 h^{-1}, 1–2‰ acetone in air)	Conversion of ca. 92% at 550 °C	[7]
Mg ferrite	SG[e] + SelfC[f]	Acetone (20–550 °C, GHSV = 5100 h^{-1})	T_{50} = 250 °C	[83]
Co ferrite	PSE-CVD[h]	Dimethyl ether; olefins (220–460 °C, WHSV = 45,000 mL g_{cat}^{-1} h^{-1}, 1% propene, 10% O_2, Ar balance)	T_{50} = 356 °C T_{90} = 409 °C	[65]
$Ni_{0.5}Co_{0.5}Sc_xFe_{2-x}O_4$ (x = 0.05; 0.1 and 0.2)	SG[e] + SelfC[f]	Benzene (50–550 °C GHSV = 5100 h^{-1}, 1–2‰ benzene in air)	Conversion of ca. 67% at 550 °C	[7]
Mg ferrite	SG[e] + SelfC[f]	Benzene (20–550 °C, GHSV = 5100 h^{-1})	T_{50} = 425 °C	[83]
$Ni_{0.5}Co_{0.5}Sc_xFe_{2-x}O_4$ (x = 0, 0.05, 0.10, and 0.20)	SG[e] + SelfC[f]	Pb-free gasoline vapors (50–600 °C, 1–2‰ gasoline in air, gas flow = 3 cm^3 s^{-1})	T_{50} = 360 °C for $Ni_{0.5}Co_{0.5}Sc_{0.2}Fe_{1.8}O_4$	[90]

[a] *SolC* solution combustion
[b] *TD* thermal decomposition
[c] *SSR* solid-state reaction
[d] *CoPP* coprecipitation
[e] *SG* sol-gel synthesis
[f] *SelfC* self-combustion
[g] *CitP* citrate precursor
[h] *PSE-CVD* pulsed spray evaporation chemical vapor deposition
[i] *HT* hydrothermal synthesis

The study of electrical conductivity could provide evidence in support of their catalytic properties in VOC combustion reactions [38]. When a *p*-type semiconductor is exposed to oxygen, its electrical conductivity increases compared to that in an inert atmosphere, due to the creation of holes (charge carriers) simultaneously with new oxygen anions in the lattice, according to the equation [38]:

$$O_{2(gas)} \Leftrightarrow O^{-}_{2(ads)} + h^{+} \Leftrightarrow 2O^{-}_{(ads)} + h^{+} \Leftrightarrow 2O^{2-}_{(ads)} + 2h^{+} \Leftrightarrow 2O^{2-}_{lattice} \quad (1.2)$$

where h^+ denotes a positive hole. However, if the same *p*-type semiconductor is exposed to a reducing atmosphere, e.g., methane, lattice oxygen is consumed and oxygen vacancies are formed, with electrons released in the valence band and the number of positive holes diminishing, therefore decreasing the electrical conductivity. For the *n*-type semiconductors, the inverse mechanism is observed: exposure to oxygen leads to electrons from the conduction band (charge carriers in this case) being consumed, therefore decreasing the electrical conductivity, while exposure to methane consumes some of the lattice oxygen, with the electrons being released into the conduction band and leading to higher electrical conductivity [38].

Popescu et al. [38] used in situ electrical measurements of some manganese-modified copper ferrites to study the correlation between the catalytic activity in methane total oxidation and their redox properties. The $CuFe_{2-x}Mn_xO_4$ spinels (x = 0; 0.4; 0.8; 1.2; 1.6; and 2) were prepared by solid-state reactions between CuO, Fe_2O_3, and Mn_2O_3 oxides, at 800 °C. $CuFe_2O_4$ and $CuMn_2O_4$ nanocrystalline spinels were identified in the XRD patterns, together with smaller amounts of individual oxides as side phases. The catalytic activity expressed as both the temperature corresponding to 10% methane conversion and the specific reaction rates at 710 °C decreased with increasing x, indicating a detrimental effect of manganese incorporation. The authors determined that as Mn is introduced in the structure the activation energy increases up to x = 0.8, then decreases with increasing x, while the pre-exponential factor varies in the opposite way accounting for the decreasing density of the active sites. This compensation effect explains the decrease of the specific catalytic activity when manganese concentration is increased [38]. From electrical conductivity measurements, $CuFe_2O_4$ was determined to be a *p*-type semiconductor, while $CuMn_2O_4$ an *n*-type semiconductor. The ternary spinel catalysts show both types of conduction mechanisms, with one type predominant as a function of temperature: at temperatures below ca. 500 °C they behave as *n*-type semiconductors, while at higher temperatures as *p*-type [38]. Since the transition from *n*- to *p*-type took place at temperatures lower than those needed for 50% methane conversion, all the ternary spinels were of *p*-type in the reaction temperature domain. For $CuFe_2O_4$, the presence of the two competing conduction mechanisms was explained [24] by the simultaneous existence of electrons (e^-) and holes (h^+) as charge carriers:

$$Fe^{2+} \leftrightarrows Fe^{3+} + e^{-} \tag{1.3}$$

$$Cu^{2+} \leftrightarrows Cu^{+} + h^{+} \tag{1.4}$$

The kinetics of these two reactions determine the type and concentrations of the charge carriers, and hence, the conduction mechanism [6, 38].

Electrical conductivity measurements under conditions as close as possible to those of catalysis (640 °C, sequential periods under air, under methane-air reaction mixtures, and under methane-nitrogen mixtures) were performed for the $CuFe_{2-x}Mn_xO_4$ with $x = 0$; 0.8 and 2 (Fig. 1.2) [38]. Under air, for $x = 0$ and 0.8, an *n*-type character was observed, while for $x = 2$ the behavior corresponded to the *p*-type. Notably, when methane was contacted with the samples, the nature of the semiconductivity changed for all three samples: those with $x = 0$ and 0.8 switched from *p* to *n*-type, while $CuMn_2O_4$ passed from *n* to *p*-type.

For the solids with $x = 0$ and 0.8, these variations were reversible when the atmosphere was changed again to air. This "breathing" behavior was explained by the oxidation of methane with lattice oxygen anions from the solid surface, leading to a partially reduced surface on which anion vacancies were created, in agreement with a Mars-van Krevelen mechanism. The free electrons thus produced are released into

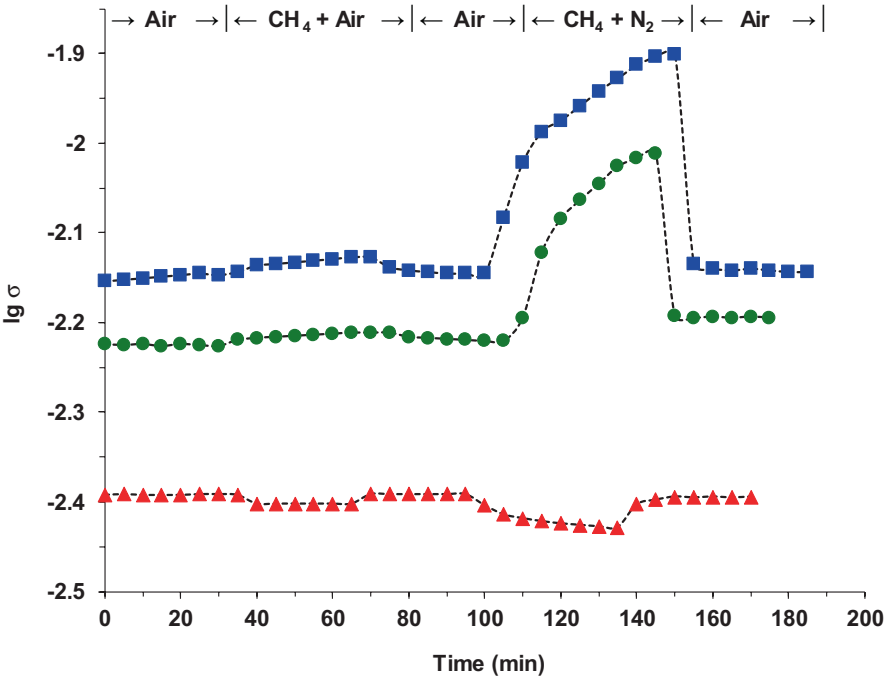

Fig. 1.2 Variation of the electrical conductivity under sequential exposures to air, methane–air mixture (reaction mixture), and methane–nitrogen mixture for $CuFe_2O_4$ (■), $CuFe_{1.2}Mn_{0.8}O_4$ (●), and $CuMn_2O_4$ (▲) at 640 °C (σ in $ohm^{-1}\ cm^{-1}$). (Reproduced from ref. [38] with permission)

the conduction band, thus increasing the electrical conductivity for the *n*-type semiconductors. When contacted with air again, the electrical conductivity values decrease, indicating that the free electrons are used for the formation of lattice oxygen anions by dioxygen dissociation, thus refilling the anion vacancies (Fig. 1.2). Similar conclusions were obtained by Munteanu et al. [6] in a study of propane combustion on $CuFe_2O_4$.

In the case of $CuMn_2O_4$ ($x = 2$), which is a *p*-type semiconductor with holes as charge carriers, each positive hole can be considered an electron vacancy in the valence band of the lattice oxygen anions or, from a chemical point of view, an O^- lattice species. This species can also activate methane molecules, and oxygen vacancies are generated again when water and CO_2 are produced. These vacancies are consistent with the observed reduction of the solid in methane-air and methane-nitrogen atmospheres, and they are filled when gaseous oxygen reoxidizes the solid. This is similar with a Mars-van Krevelen mechanism, but involving O^- lattice species in line with the *p*-type character of the solid. However, due to the smaller variations of the electrical conductivity values observed for this catalyst, the authors suggested a low concentration of O^- species for this solid, therefore explaining its low catalytic activity. As a conclusion, the in situ electrical conductivity measurements provided clear and direct evidence for a redox mechanism in which surface lattice oxygen from the spinel solid is consumed, which can be assimilated to a Mars-van Krevelen mechanism [38].

1.3 Manganese-Based Spinel Catalysts

Mn-based spinels are active in NO reduction [94], NO decomposition [95], water gas-shift reaction [96], methanol reforming [97], CO oxidation [98–100], and combustion of VOC [101, 102] such as methane [4], propane [99], ethylene [103], propylene [103], benzene [104, 105], toluene [100, 104, 106, 107], *o*-xylene [105], and 2-propanol [108, 109].

Mn_3O_4 has a normal spinel structure, with tetrahedral sites occupied by Mn^{2+} ions, and Mn^{3+} ions placed in distorted octahedral sites [103, 104]. $CuMn_2O_4$ shows a normal spinel structure with cubic [110] or slightly tetragonal symmetry [111], reflecting the Jahn-Teller distortion that depends on the concentration of Mn^{3+} and Cu^{2+} ions in octahedral sites. The tetragonal structure has an axial *c/a* ratio slightly higher than unity but very close to it, which decreases towards 1 with increasing thermal treatment temperature [111]. $NiMn_2O_4$ has a cubic spinel structure [108], and so do $Co_xMn_{3-x}O_4$ spinels with $x > 0.9$ [99].

1.3.1 Preparation Methods

The preparation methods of manganites are similar to those already discussed for ferrites:

- Coprecipitation [4, 100, 105, 109, 112, 113] is a commonly used method that usually starts from nitrates [4, 100, 109, 112, 113], but also from acetates [113] or chlorides [105] and uses NaOH [4, 100, 112], alkaline carbonates [105, 109], or tetramethylammonium hydroxide (TMAH) [113] as precipitating agents. An alternative of this method, the redox-precipitation procedure, uses $KMnO_4$ as oxidant [105, 113]. The redox-precipitation method leads to metal cation loss (e.g., Cu^{2+}) due to the fact that these cations are not involved in the redox reaction; therefore, a high Mn/M ratio is obtained in the final solid, far exceeding the value of 2 obtained by coprecipitation [113]. Also, minor side phases such as CuO [113] were reported besides the expected spinel. In some cases [105], the redox-precipitation does not lead to spinel mixed oxides, but to a mixture of oxides with different structures. To obtain solids with high specific surface areas, silica aquagel confined coprecipitation (SACOP) procedure uses a sodium silicate solution to obtain a high dispersion of the metallic cations in the silica aquagel. During calcination that takes place confined inside the pores of the silica matrix, the growth of the solid nanoparticles is restricted and, hence, high surface areas are obtained. The silica matrix is removed in a final step by dissolution in NaOH solution [112];
- Solid-state reaction [104, 111] starts from the corresponding oxides that are sintered at high temperatures in order for the spinel to be formed;
- Chemical complexation method uses metal salts (e.g., nitrates [99] or acetates [114]) and an organic acid such as $H_2C_2O_4$ [99, 114, 115]. The specific surface area and the particle size of the spinel depend on the conditions used for the decomposition of the precursor (oxalate) [99, 114];
- Sol-gel method uses metal nitrates and citric acid [108] or glycine [109] to obtain a gel. The procedure may include a self-combustion step that increases the temperature above 1000 °C for a short time when the gel is heated [108, 109]. Although the method is used for obtaining pure-phase mixed oxides [109], minor impurity phases containing single oxides such as CuO and NiO were sometimes reported [108];
- Solution combustion synthesis uses salts (e.g., nitrates) as oxidants and a fuel (e.g., $C_2H_5NO_2$) as reducing agent. The homogeneous solution of the two reagents is heated in an oven at constant temperature for the reaction to take place, then the resultant powder is washed and dried. Pure spinel phase was reported for this method [103];
- Dispersion-precipitation method is a modified precipitation procedure that uses glacial acetic acid added after precipitation to the obtained slurry to form a stable homogeneous dispersion of nanoparticles; in the second step, the suspension is diluted with water and precipitation gradually occurs by agglomeration of the nanoparticles [100];

– Spray deposition followed by thermal decomposition [110] starts with a solution of salts (e.g., nitrates) that is sprayed at temperatures above 400 °C on a surface (e.g., quartz plate) and heated afterwards at high temperatures for the decomposition to take place completely.

1.3.2 Mn_3O_4

Toluene combustion was studied on Mn_3O_4 obtained by the dispersion-precipitation (DP) method [100]. When compared with Mn_3O_4 obtained by direct precipitation (P) or by decomposition of manganese acetate (D), the solid obtained by DP method showed smaller particle size (5–25 nm compared to 30–55 nm and more than 200 nm, respectively) and larger specific surface areas (110 $m^2\ g^{-1}$, compared to 37 and 5 $m^2\ g^{-1}$, respectively), better reducibility and, therefore, higher catalytic activity in toluene total oxidation. T_{90} for the three catalysts were 245 °C, 260 °C, and 280 °C, respectively. The smaller particle size and better reducibility of the catalyst synthesized by the DP method accounted for its higher activity.

Combustion of benzene and toluene was investigated on 0.5 wt. % K, Ca, or Mg-modified Mn_3O_4 catalysts obtained by impregnation followed by calcination [104]. All modified samples showed better activity for the combustion of toluene than the parent Mn_3O_4: T_{50}/T_{90} values were 230/250 °C for both 0.5% K/Mn_3O_4 and 0.5% Ca/Mn_3O_4, and 232/255 and 245/270 °C for 0.5% Mg/Mn_3O_4 and Mn_3O_4, respectively. When benzene was used, T_{50} and T_{90} values were shifted by 10–20 °C to lower temperatures, indicating that benzene is more easily combusted than toluene. When benzene-toluene mixtures were tested, a mutual inhibitory effect was observed and the conversion curves were shifted to higher temperatures. A strong correlation between the conversion values and the presence of a hydroxyl-like group defect with higher mobility than the lattice oxygen in the manganese oxide structure was observed, detected by XPS and TPR. This defect was present in higher concentrations in the promoted catalysts; therefore, it has been concluded that K, Ca, and Mg have an important role in the formation of the mentioned defect.

Mn_3O_4 spinel prepared by solution combustion synthesis, together with other manganese oxides (Mn_2O_3 and Mn_xO_y—a mixture of Mn_2O_3 and MnO_2 phases), were tested in the total oxidation of some VOC test molecules: ethylene, propylene, toluene, and their mixture [103]. O_2-TPD and XPS experiments showed the presence of both chemisorbed oxygen (O^- and O_2^-, named α species, with high mobility) and structural oxygen (named β-species) in Mn_3O_4, which exhibited higher O_α/O_β ratio compared to the other manganese oxides. FTIR spectroscopy by means of NH_3 adsorption at room temperature indicated the presence of different types of hydroxyl groups on the surface of Mn_3O_4, and also Mn sites acting as Lewis acid centers. At higher temperatures, the surface hydroxyls can be converted into Lewis acid sites by dehydroxylation, while water interaction with such centers reconverts them into hydroxyls. These nanodefects on the surface can favor oxidation reactions, especially at low temperatures (below 400 °C). The order of activity for all individually

tested VOC and for their mixture was $Mn_3O_4 > Mn_2O_3 > Mn_xO_y$. A Mn_3O_4-based monolith was prepared by solution combustion synthesis and showed comparable performances to the Mn_3O_4 powder, which were stable for 10 h on stream without deactivation. The authors highlighted the importance of the surface defects leading to a high amount of adsorbed oxygen species on the surface (α species) that promote total oxidation.

1.3.3 Cu–Mn Spinels

The valence state of copper and manganese ions in $CuMn_2O_4$ was investigated by Ghare et al. [110], Gillot et al. [111], and by Valdes-Solis et al. [112] in order to clarify if copper is present as Cu^+ or Cu^{2+} in the structure. Ghare et al. [110] studied the spinel structure by electrical conductivity and differential thermal analysis methods, while Gillot et al. [111] and Valdes-Solis et al. [112] used XPS and FTIR spectroscopy measurements. While literature proposed either the formula $Cu^+[Mn^{3+}Mn^{4+}]O_4$ or $Cu^{2+}[Mn^{3+}{}_2]O_4$, Ghare et al. [110] were able to observe that at ca. 600 K the following transformation occurs:

$$Cu_A^{\ +} + Mn_B^{\ 4+} \leftrightarrows Cu_B^{\ 2+} + Mn_A^{\ 3+} \tag{1.5}$$

that was identified as a source of high activity in oxidation reactions [107, 112]. This modification in valence states accounted for a change of the slope in $\log R = f(1/T)$ plots (R = resistivity, the inverse of conductivity) and a small endothermic change in the DTA curve. It has been concluded that both formulas are correct, but at different temperatures. In $Cu^+[Mn^{3+}Mn^{4+}]O_4$, the numbers of Mn^{3+} and Mn^{4+} ions are equal, so the number of charge carriers is large and, hence, the activation energy of conduction is low; this feature was observed at low temperatures. For $Cu^{2+}[Mn^{3+}{}_2]O_4$, all octahedral positions are occupied by Mn^{3+}, so the number of charge carriers is small and, consequently, the activation energy of conduction is high; this behavior was observed above 600 K. Therefore, Ghare et al. [110] concluded that the solid behaves as $Cu^+[Mn^{3+}Mn^{4+}]O_4$ at temperatures up to 600 K and changes to $Cu^{2+}[Mn^{3+}{}_2]O_4$ above this value. XPS and FTIR measurements performed by Gillot et al. [111] on samples treated at 850–930 °C and then rapidly quenched showed the presence of Cu^+ in tetrahedral sites and Cu^{2+} (in lower amount) in octahedral sites, which led to the conclusion that, regardless of the preparation temperature, most copper ions are placed in tetrahedral positions and are monovalent, with the Cu^+/Cu^{2+} ratio close to 1.5. Another electronic exchange that influences the electronic configuration has been identified:

$$Mn_A^{\ 3+} + Mn_B^{\ 3+} \leftrightarrows Mn_A^{\ 2+} + Mn_B^{\ 4+} \tag{1.6}$$

the ionic configuration being best represented by the formula:

$$\left(Cu^{+}_{\alpha}Mn^{2+}_{\beta}Mn^{3+}_{1-\alpha-\beta}\right)_{A}\left(Cu^{2+}_{1-\alpha}Mn^{3+}_{1-\beta}Mn^{4+}_{\alpha+\beta}\right)_{B}O^{2-}_{4}$$

The XPS spectra of the $CuMn_2O_4$ prepared by Valdes-Solis et al. [112] with the silica aquagel confined coprecipitation method also showed the presence of Cu^+ and Mn^{2+} in tetrahedral positions, while Cu^{2+}, Mn^{3+}, and Mn^{4+} were identified in octahedral sites, but no Mn^{3+} was observed in tetrahedral positions.

A study about the influence of the preparation variables on the properties of $CuMn_2O_4$ was published by Hutchings et al. [98]. The investigated variables were: precipitate aging time (30 min–24 h), pH (7.5–10.0), and temperature (25–80 °C) of the precipitation, [Cu]/[Mn] ratio in the initial solution (from 100% Cu to 100% Mn), and calcination temperature (300–800 °C). The unaged precursor obtained during precipitation was identified as a mixture of copper hydroxyl nitrate and manganese carbonate, hence Cu and Mn are found in separate phases. During aging, the $CuMn_2O_4$ was formed together with CuO. The BET surface areas were not influenced by the aging time or aging temperature, but by pH and the [Cu]/[Mn] ratio. The Cu/Mn ratio in the bulk is significantly influenced by the pH of the precipitation step, since the onset for Cu^{2+} and Mn^{2+} precipitation from solution is found at 7 and 8, respectively, and higher pH is needed for a complete precipitation of Mn^{2+}. At pH = 7.5, a Cu-rich amorphous solid was produced, while at higher pH values Cu-Mn spinels were obtained together with Mn_2O_3 and CuO secondary phases. The composition of the initial solution also has a marked influence, with the stoichiometric ratio leading to the desired spinel. Calcination at low temperatures (300 °C) leads to poorly crystalline $MnCO_3$ and CuO, and at 500 °C, $CuMn_2O_4$ was formed. At higher temperatures, $Cu_{1.4}Mn_{1.6}O_4$ and, then, $Cu_{1.2}Mn_{1.8}O_4$ phases were identified, together with a Mn_2O_3 minority phase. The optimum parameters for the synthesis were found to be 12 h aging time, pH = 9, precipitation temperature of 80 °C, [Cu]/[Mn] = 1/2, and calcination temperature of 500 °C.

While studying catalytic methane combustion over Cu-(Mn)-Zn-Mg-Al mixed oxides obtained from layered double hydroxides (LDH) precursors, Răciulete et al. [4] observed the formation of some spinel phases. Four Cu(Mn)ZnMgAl-LDH precursors were prepared by coprecipitation, with (Cu + Mn + Zn + Mg)/Al atomic ratio equal to 3, Cu/Zn = 1 and Mn/Cu = 0, 0.5, 1, and 2. During the thermal decomposition of the LDH precursors, several spinel phases were identified, such as $Cu_{1.5}Mn_{1.5}O_4$ and $CuMn_2O_4$. When solids with Mn/Cu = 1 were further studied for the influence of the calcination temperature, the formation of the spinel phases was already observed at 550 °C, besides the periclase-like mixed oxide phase, and increasing the thermal treatment temperature up to 800 °C resulted in a higher crystallinity (Fig. 1.3). TPR studies showed that the reduction of copper in these solids is promoted by the presence of manganese, while XPS spectra confirmed the presence of Cu and Mn species with different valence states and the formation of $Cu_{1.5}Mn_{1.5}O_4$ spinel [4]. In catalytic methane combustion tests, the incorporation of manganese strongly increased the activity up to Mn/Cu = 1, but only this latter sample was able to lead to high methane conversion values (94% at 640 °C) (Fig. 1.4.). It has been suggested that at temperatures below 500 °C, the active phases are CuO

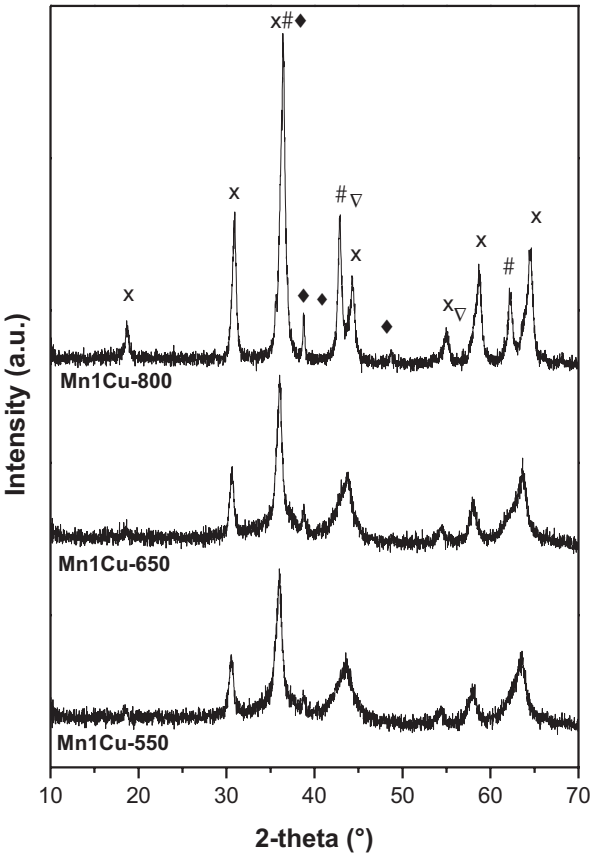

Fig. 1.3 XRD patterns of Mn1Cu-*T* mixed oxide catalysts calcined at different temperatures. Symbols: ×—$Cu_{1.5}Mn_{1.5}O_4$, $MnAl_2O_4$, and $CuMn_2O_4$, ◆—CuO, #—periclase-like phase. (Reproduced from ref. [4] with permission)

and $Cu_{1.5}Mn_{1.5}O_4$, while the $CuMn_2O_4$ spinel becomes active only at higher temperatures. The high intrinsic activities observed were associated with a high reducibility both in terms of hydrogen consumption and easiness of reduction, related to the presence of $Cu_{1.5}Mn_{1.5}O_4$ spinel [4].

$Cu_xMn_{2-x}O_4$ ($0 < x < 1$) spinels prepared using an alginate precursor were used by Behar et al. [107] for the complete oxidation of toluene as model VOC. Alginate is a natural polysaccharide with carboxylic groups, extracted from brown algae, which has a high affinity for divalent cations and provides nanoscale oxide dispersion and relatively high specific surface areas. $Cu_{1.5}Mn_{1.5}O_4$ spinel was obtained when the [Cu]/([Cu] + [Mn]) ratio in the initial solution varied from 0.1 to 0.57, together with Mn_3O_4 (for $x = 0$) and variable amounts of CuO (for $x > 0.7$). The high activity of the $Cu_{1.5}Mn_{1.5}O_4$ spinel in toluene combustion was correlated with its low reduction temperature, starting at 130 °C, and the presence of Cu^+/Cu^{2+} and $Mn^{3+}/$

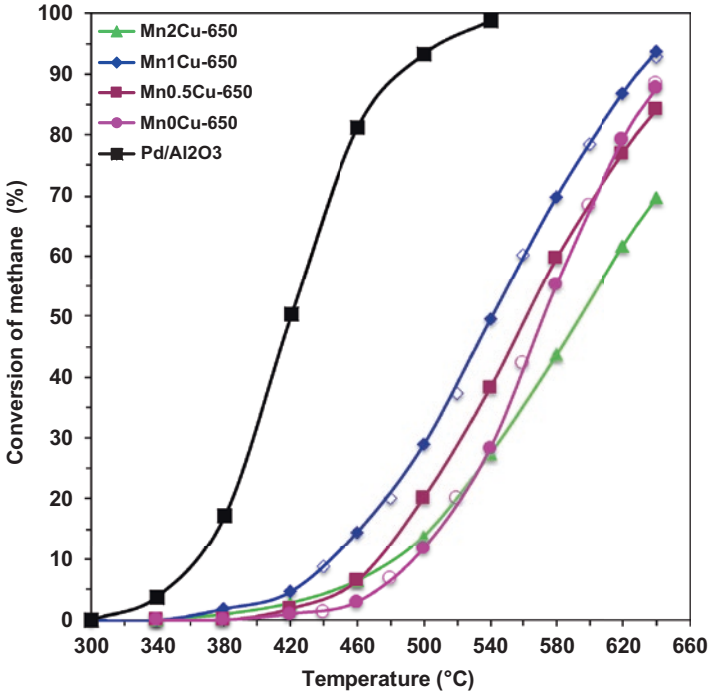

Fig. 1.4 The light-off curves for the combustion of methane over Mn*X*Cu-650 (open symbols correspond to the second light-off test). (Reproduced from ref. [4] with permission)

Mn^{4+} redox systems. However, when $Cu_{1.5}Mn_{1.5}O_4$ spinel was supported on TiO_2, its catalytic activity decreased, likely due to an inhibition effect of the support. A kinetic study [116] showed that the Mars-van Krevelen model describes the total oxidation of toluene on $Cu_{1.5}Mn_{1.5}O_4$ better than other kinetic models, such as power law and Langmuir-Hinshelwood.

The same $Cu_{1.5}Mn_{1.5}O_4$ spinel was prepared by coprecipitation [105] and tested, together with other Cu-Mn mixed oxides with different structures, in the complete oxidation of benzene, toluene, and *o*-xylene. Although the performances of the $Cu_{1.5}Mn_{1.5}O_4$ spinel were lower compared with the other tested catalysts, it showed reasonably good activity: T_{90} for benzene, toluene, and *o*-xylene were 295 °C, 280 °C, and 286 °C, respectively. However, CO was produced besides CO_2, which was related to a poor activity for CO oxidation. Slow deactivation was observed for long time on stream, while the presence of water, SO_2, and CO_2 had an important inhibiting effect, which was reversible in the case of water. It has been concluded that the presence of surface oxygen species and oxygen vacancies, observed by XPS and H_2-TPR measurements, plays a major role in the catalytic combustion of VOC.

Vu et al. [106] studied toluene combustion on $Cu_yMn_{1-y}O_x$ mixed oxides (y = 0, 0.25, 0.33, 0.50, 0.66, 0.75, 1.0) obtained by incipient wetness impregnation of Cu and Mn nitrates on a TiO_2 support, followed by calcination. Formation of

$Cu_{1.4}Mn_{1.6}O_4$ mixed spinel was identified by XRD in all samples except for Mn_2O_3 ($y = 0$) and CuO ($y = 1$). A decrease of specific surface area with increasing the Cu content (y values) was noticed. On all the catalysts, toluene was completely and selectively converted into CO_2 at temperatures above 250 °C, with conversion values maintained at 100% for 14 h on stream. However, at lower temperatures, the conversion decreased due to deactivation: at 200 °C, it reached 48% after 1 h and 21% after 4 h, but the activity could be completely restored by treatment in air at 300 °C. A direct correlation between the presence of the $Cu_{1.4}Mn_{1.6}O_4$ spinel in higher proportion and the high activity in toluene conversion was observed.

The influence of the preparation method on the performances of $CuMnO_x$ mixed oxides in the total oxidation of toluene was studied by Ye et al. [113]. The Cu-Mn oxides were prepared either by coprecipitation using tetramethylammonium hydroxide ($CuMn_2O_4$), or by redox-precipitation with $KMnO_4$ ($CuMnO_x$). The second method ensured a better dispersion of copper in close interaction with manganese, providing more active sites at the surface and, hence, a higher activity was obtained compared with $CuMn_2O_4$ prepared by coprecipitation or with the single Cu and Mn oxides. Copper was detected by XPS to be present both as Cu^+ and Cu^{2+}, with a Cu^+/Cu^{2+} ratio close to 0.5 in $CuMn_2O_4$, while manganese was present as Mn^{3+} and Mn^{4+}, the latter being predominant. Surface oxygen species with low coordination (surface oxygen vacancies) were also observed by XPS in high concentration in solids obtained by both methods. The order of activity for total oxidation of toluene was $CuMnO_x > CuMn_2O_4 > MnO_x > CuO_x$. The good performance of the catalysts obtained by the redox route was ascribed to improved textural properties such as high specific surface areas, amorphous state, and presence of oxygen vacancies. The oxidation of toluene was observed to occur also in the absence of gaseous oxygen and was attributed to the participation of surface and lattice oxygen species. XRD patterns of the catalysts after the reaction without gaseous oxygen revealed the presence of MnO and Cu^0 for $CuMn_2O_4$, while $Cu_{0.1}Mn_{2.9}O_4$ and $Cu_{1.5}Mn_{1.5}O_4$ were observed for $CuMnO_x$. It is worth noting that the $Cu_{1.5}Mn_{1.5}O_4$ active phase was also observed in other studies [4, 105, 116] (see above). Some organic reaction intermediates were observed by ToF-SIMS spectroscopy, such as benzene, phenol, benzaldehyde, and benzoic acid [113]. All the catalysts deactivated with time on stream, but modifying them with 0.5% Pd or Pt by impregnation allowed a better resistance to deactivation, without improving activity.

1.3.4 Co-Mn Spinels

Castaño et al. [109] studied the influence of the synthesis method on the performances of some Co-Mn spinel mixed oxides in the total oxidation of 2-propanol and toluene. The solids were prepared by coprecipitation (CP) or self-combustion (SC) of hydrotalcite-type precursors in order to obtain high specific surface areas and good inter-dispersion of the cations. The prepared catalysts contained simple spinel structures of Mn and Co and mixed $Co_xMn_{3-x}O_4$ ($x = 1$ or 2) spinel oxides. Those

prepared by SC method showed smaller particle sizes, but also smaller specific surface areas and larger pores compared to those prepared by CP. The latter method seemed to favor oxygen mobility due to a cooperative effect between Mn and Co cations. The results demonstrate the fundamental role of the synthesis method on the oxygen mobility and, therefore, on the catalytic activity. In the total oxidation of 2-propanol, the catalysts derived from CP procedure had a lower T_{90} (242 °C, compared to 262 °C for SC), while in toluene complete oxidation they behaved similarly (T_{90} = 280 °C). In combustion tests of both compounds, the co-precipitated solids showed better performance than the single Mn and Co oxides, while those prepared by SC were intermediary between the manganese oxide and the cobalt oxide. Three complementary factors determined the catalytic behavior of the studied catalysts: oxygen mobility, redox properties, and oxygen species, both adsorbed on the surface (O_2^- and O^-), and lattice oxygen ions (O^{2-}), whose presence was demonstrated by O_2-TPD, ^{18}O isotope exchange, and H_2-TPR.

$Co_xMn_{3-x}O_4$ ($0 \leq x \leq 3$) spinels were prepared by controlled thermal decomposition of mixed oxalates and tested in the total oxidation of propane [99]. The synthesis method ensured large specific surface areas due to restrained shrinkage of the crystallites during thermal treatment, the highest value being obtained for x = 1.6 (270 $m^2\ g^{-1}$). At x values above 0.9, the activity in propane combustion starts to increase, up to x = 2.3; $Co_{2.3}Mn_{0.7}O_4$ showed the best performance, with complete conversion of C_3H_8 at 300 °C. Stability tests for this composition indicated the conversion was stable for 14 h on stream at 160 °C. The obtained results were explained by the presence of catalytically active Co^{3+} ions in octahedral sites: at low x values, the activity is not influenced much because the substitution of Mn with Co takes place in the inactive tetrahedral sites, but when these sites are fully occupied by Co^{2+} (at $x > 1$) the substitution continues in the octahedral sites, where Mn^{3+} is replaced by Co^{2+} and Co^{3+}. It is worth noting that, for each Co^{2+} in an octahedral site, the oxidation of one Mn^{3+} to Mn^{4+} takes place in order to preserve the lattice neutrality. A similar study by Tang et al. [115] concerning total oxidation of ethyl acetate and hexane over Co-Mn spinel obtained from oxalate decomposition reached the same conclusions: the high specific surface area and small particle size led to a better performance than that of the single Mn or Co oxides, and complete oxidation for the two model compounds was achieved under 230 °C.

$Co_xMn_{3-x}O_4$ spinel catalysts with different Mn/Co atomic ratios (1:1, 1:2, 1:4, 2:1 and 4:1) were also studied by Huang et al. [117] for the total oxidation of formaldehyde at low temperatures. The solids were prepared by anodic electrodeposition on a flexible carbon textile substrate from a solution of manganese nitrate, cobalt chloride, and dimethyl sulfoxide at 70 °C, followed by the annealing of the Co-Mn precursor nanosheets in air at 550 °C. By adjusting the Mn/Co ratio in the initial electrolyte, x was varied between 0.43 and 0.78 in the final spinel structures. The $Co_{0.65}Mn_{2.35}O_4$ sample had the highest amounts of Co^{3+} content and adsorbed oxygen on the surface, a significant increase in reducibility compared to the other spinels, and more oxygen vacancies on the surface. It was concluded that all these properties account for its highest performance among the investigated spinels and single Mn and Co oxides, i.e., 100% HCOH conversion at 100 °C. The order of

activity and the temperatures for complete oxidation of formaldehyde followed the order: $Co_{0.65}Mn_{2.35}O_4$ (100 °C) > $Co_{0.70}Mn_{2.30}O_4$ (110 °C) > $Co_{0.58}Mn_{2.42}O_4$ (130 °C) > $Co_{0.78}Mn_{2.22}O_4$ (140 °C) = $Co_{0.43}Mn_{2.57}O_4$ (140 °C) > MnO_x (170 °C) > CoO_x (180 °C). The $Co_{0.65}Mn_{2.35}O_4$ catalyst also showed excellent stability for 300 h on stream, even in humid atmosphere. A mechanism was proposed for the process that includes oxidation of formaldehyde to formate and hydrocarbonate species, which decompose to CO_2 and water.

Copper, nickel, and cobalt manganites prepared by the sol-gel self-combustion method were used in the total oxidation of two model VOC compounds, i.e., toluene and 2-propanol [108]. For both molecules, the order of activity was $NiMn_2O_4$ > $CuMn_2O_4$ > $CoMn_2O_4$, the better performance of nickel manganite being attributed to a higher content of Mn^{3+} and a synergetic effect between manganese and nickel in the spinel structure. Toluene was completely oxidized at 350 °C on $NiMn_2O_4$, while for 2-propanol a temperature of 250 °C was necessary on the same catalyst.

Cobalt manganite prepared by chemical complexation with oxalic acid was studied in the toluene combustion process and proved to be more active than the metal oxides, either single (Co_3O_4, MnO_x) or the mixed oxide Co_3O_4/MnO_x obtained by impregnation [114]. The authors claimed that the high performance was due to a larger specific surface area and abundant defects in the spinel structure, leading to a higher number of active sites for toluene adsorption and activation. Co^{2+}, Mn^{3+}, Mn^{4+}, chemisorbed oxygen, and a high number of oxygen vacancies were identified in the spinel by XPS. $CoMn_2O_4$ showed a better stability compared with the other oxides, with conversion values above 98% at 220 °C for 700 min in the presence or absence of water vapor (2%). The surface lattice oxygen was proposed to be the main active oxygen species in the catalytic reaction, an observation similar with that of Piumetti et al. [103] and Ye et al. [113], while migration of bulk lattice oxygen promotes the formation of the surface oxygen species. This claim was supported by the fact that the combustion reaction continued for the spinel for more than 45 min after the oxygen supply was stopped. When oxygen was reintroduced in the feed, the oxygen vacancies were replenished and the activity recovered. From the reaction intermediates identified by DRIFT spectroscopy, the authors concluded that toluene combustion takes place on $CoMn_2O_4$ through a benzyl alcohol—benzoic acid—maleic anhydride—acetic acid pathway, finally leading to CO_2 and H_2O, with anhydride conversion identified as the rate-controlling step. It was shown that the Co_3O_4/MnO_x mixed oxide catalyzes the combustion reaction on a different pathway due to low migration of bulk oxygen to the surface and benzoate dissociation as the rate-controlling step. The differences in structure and reducibility between $CoMn_2O_4$ and the other Co-Mn oxides result in different oxygen mobility from bulk to surface and number of active oxygen species and, hence, different catalytic performances [114].

Table 1.2 summarizes the different manganite spinel catalysts hereby described together with their preparation methods and catalytic applications in VOC combustion.

Table 1.2 Preparation and catalytic performance of the manganite spinel catalysts in VOC total oxidation

Catalyst	Preparation method	Tested chemical compound (reaction conditions)	Best results	Ref.
$Cu_{1.5}Mn_{1.5}O_4$ in a periclase-like matrix	TD[a] of LDH precursors	Methane (300–660 °C, 1% CH_4 in air, GHSV = 20,000 h^{-1})	94% conversion at 640 °C	[4]
Mn_3O_4	SolC[b]	Ethene (100–350 °C, 1000 ppm ethene in air, GHSV = 19,100 h^{-1}, W/F = 0.03 g h L^{-1})	T_{100} = 265 °C	[103]
$Co_xMn_{3-x}O_4$ ($0 \leq x \leq 3$)	TD[a] of oxalate precursors	Propane (30–300 °C, 0.4% propane, 20% O_2 in Ar, 1.63 mL s^{-1})	T_{100} = 300 °C on $Co_{2.3}Mn_{0.7}O_4$	[99]
Mn_3O_4	SolC[b] synthesis	Propene (100–350 °C, 1000 ppm propene in air, GHSV = 19,100 h^{-1}, W/F = 0.03 g h L^{-1})	T_{100} = 250 °C	[103]
Co manganite	TD[a] of oxalate precursors	Hexane (100–250 °C 1000 ppm hexane in air, 100 mL min^{-1}, 120,000 mL g^{-1} h^{-1})	T_{100} = 230 °C	[115]
Mn_3O_4 doped with 0.5 wt. % K, Ca, and Mg	IMP[c] of Mn_3O_4 with K, Ca, or Mg nitrates, followed by calcination	Benzene (200–400 °C, 2000 ppm C_6H_6 in air, 100 mL min^{-1})	T_{100} = 260 °C on 0.5% Ca/Mn_3O_4	[104]
$Cu_{1.5}Mn_{1.5}O_4$	CoPP[d]	Benzene (200–350 °C, 500 ppm benzene in humid air, 200 mL min^{-1}, GHSV = 100,000 h^{-1})	T_{90} = 295 °C	[105]
Mn_3O_4	SolC[b] synthesis	Toluene (100–350 °C, 1000 ppm toluene in air, GHSV = 19,100 h^{-1}, W/F = 0.03 g h L^{-1})	T_{100} = 265 °C	[103]
Mn_3O_4	DPP[e] method	Toluene (180–300 °C, 1000 ppmv toluene in air, GHSV = 180,000 h^{-1})	T_{90} = 245 °C	[100]

(continued)

Table 1.2 (continued)

Catalyst	Preparation method	Tested chemical compound (reaction conditions)	Best results	Ref.
Mn_3O_4 doped with 0.5 wt. % K, Ca, and Mg	IMP[c] of Mn_3O_4 with K, Ca, or Mg nitrates, followed by calcination	Toluene (200–400 °C, 2000 ppm toluene in air, 100 mL min^{-1})	T_{100} = 280 °C on 0.5% Ca/Mn_3O_4	[104]
$Cu_yMn_{1-y}O_x$/TiO_2 (y = 0, 0.25, 0.33, 0.50, 0.66, 0.75, 1)	IWI[f] of Mn and Cu nitrates on TiO_2, followed by calcination	Toluene (150–300 °C, 500 ppm toluene in air, GHSV = 5000 h^{-1})	T_{100} = 240 °C on the sample with y = 0.5	[106]
$Cu_xMn_{3-x}O_4$ ($0 < x < 1$)	Xerogels obtained via alginate hydrogel, calcined at 450 °C	Toluene (25–450 °C, 1000 ppm toluene in air, 100 mL min^{-1})	T_{50} = 239 °C, T_{100} = 315 °C on $Cu_{1.5}Mn_{1.5}O_4$	[107]
$CuMnO_x$	CoPP[d] and RedoxPP[g], calcined at different temperatures	Toluene (100–300 °C, 800 ppmv toluene in air, 100 mL min^{-1}, GHSV = 30,000 mL g^{-1} h^{-1})	T_{90} = 190 °C for $CuMnO_x$ prepared by RedoxPP and calcined at 200 °C	[113]
$Cu_{1.5}Mn_{1.5}O_4$	CoPP[d]	Toluene (200–350 °C, 500 ppm toluene in humid air, 100 mL min^{-1}, GHSV = 50,000 h^{-1})	T_{90} = 280 °C	[105]
Cu, Co, and Ni manganite	SG[h] + SelfC[i]	Toluene (150–400 °C, 0.2% toluene in air)	T_{100} = 350 °C on Ni manganite	[108]
$Co_xMn_{3-x}O_4$ (x = 1 or 2)	CoPP[d] and SelfC[i] of hydrotalcite-like precursors	Toluene (100–400 °C, 600 ppm toluene in air, 280 mL min^{-1})	T_{90} = 280 °C for $CoMn_2O_4$	[109]
Co manganite	Chemical complexation with $H_2C_2O_4$	Toluene (160–250 °C, 500 ppm toluene, 20% O_2/Ar, 75 mL min^{-1}, GHSV = 22,500, and 45,000 mL g^{-1} h^{-1})	T_{50} = 202 °C, T_{90} = 210 °C, T_{100} = 220 °C, at GHSV = 22,500 mL g^{-1} h^{-1}	[113]
$Cu_{1.5}Mn_{1.5}O_4$	CoPP[d]	*o*-xylene (200–350 °C, 200 ppm *o*-xylene in humid air, 100 mL min^{-1}, GHSV = 50,000 h^{-1})	T_{90} = 286 °C	[105]

(continued)

Table 1.2 (continued)

Catalyst	Preparation method	Tested chemical compound (reaction conditions)	Best results	Ref.
$Co_xMn_{3-x}O_4$ (x = 0.43; 0.58; 0.65; 0.70; and 0.78)	ED[h] on a carbon textile substrate, followed by annealing in air at 550 °C	Formic aldehyde (4100 mL min^{-1}, GHSV = 120,000 mL g^{-1} h^{-1})	T_{100} = 100 °C	[117]
Cu, Co, and Ni manganite	SG[i] + SelfC[j]	2-propanol (150–400 °C, 0.2% 2-propanol in air)	T_{100} = 250 °C on Ni manganite	[108]
$Co_xMn_{3-x}O_4$ (x = 1 or 2)	CoPP[d] and SelfC[j] of hydrotalcite-like precursors	2-propanol (50–400 °C, 1000 ppm 2-propanol in air, 280 mL min^{-1})	T_{90} = 242 °C for $CoMn_2O_4$ obtained by CoPP	[109]
Co manganite	TD[a] of oxalate precursors	Ethyl acetate (100–250 °C, 1000 ppm ethyl acetate in air, 100 mL min^{-1}, 120,000 mL g^{-1} h^{-1})	T_{100} = 220 °C	[115]
Mn_3O_4	SolC[b] synthesis	Ethylene + propylene + toluene (100–350 °C, 1000 ppm mixture in air, GHSV = 19,100 h^{-1}, W/F = 0.03 g h L^{-1})	T_{100} = 310 °C	[103]

[a]*TD* thermal decomposition
[b]*SolC* solution synthesis
[c]*IMP* impregnation
[d]*CoPP* coprecipitation
[e]*DPP* dispersion-precipitation
[f]*IWI* incipient wetness impregnation
[g]*RedoxPP* redox-precipitation
[h]*ED* electrodeposition
[i]*SG* sol-gel synthesis
[j]*SelfC* self-combustion

1.4 Cobalt-Based Spinel Catalysts

Supported and unsupported Co_3O_4 spinel is one of the most active mixed-valence metal oxides catalysts for the total oxidation reaction of VOC mainly due to its excellent reduction ability and high concentration of surface electrophilic oxygen species [2, 11, 15]. Introducing another metallic component into the Co_3O_4 spinel to form a binary cobaltite is an effective way to improve its combustion catalytic properties due to the synergy between the two metallic cations [118]. The most relevant papers published in the last decade focusing on Co-based spinel catalysts for complete oxidation of VOC are reviewed below.

1.4.1 Unsupported and Supported Co_3O_4

In an attempt to enhance the catalytic performance by tuning the catalyst morphology, spinel-type cobalt oxide (Co_3O_4) nanocrystals with different morphologies, i.e., cubic (C), hexagonal plate-like (P), hexagonal sheet-like (S) and flower-like (F), denoted as Co_3O_4-C, Co_3O_4-P, Co_3O_4-S, and Co_3O_4-F, respectively, were controllably prepared via a hydrothermal method [119]. Pure and highly crystalline spinel phases were obtained in all cases. In spite of their different morphologies, Co_3O_4-S, Co_3O_4-P, and Co_3O_4-F catalysts predominantly expose {111} planes, while Co_3O_4-C catalyst exposes {001} planes. The ratio between the surface-adsorbed oxygen (O_{ads}) and surface lattice oxygen (O_{latt}) species in the Co_3O_4 catalysts, determined by XPS, increases following the order: Co_3O_4-C < Co_3O_4-S < Co_3O_4-F ≈ Co_3O_4-P. Their activity in methane combustion follows the same order (Fig. 1.5), which is consistent with the fact that, in general, the lattice oxygen is involved in selective oxidation, while adsorbed electrophilic species such as O_2^{2-}, O_2^-, and O^- participate preferentially in the complete oxidation. On the other hand, the Co_3O_4 catalysts exposing dominantly {111} plane (flower-like, hexagonal plate-like, and hexagonal sheet-like) were more active than cubic Co_3O_4, which exposes mainly {001} planes.

Co_3O_4 with different morphologies was also studied in the total oxidation of formaldehyde. Thus, rod-like, sheet-like, and cube-like pure Co_3O_4 spinel catalysts were prepared by a modified precipitation for the former or a hydrothermal method for the two later [120]. As expected, the oxides have different physicochemical characteristics. Indeed, the Co_3O_4-rod sample had a significantly larger specific surface area (83.5 $m^2\ g^{-1}$) compared to that of Co_3O_4-sheet (8.5 $m^2\ g^{-1}$) and Co_3O_4-cube (3.7 $m^2\ g^{-1}$). Also, Co_3O_4-rod showed $(OH)_s/O_{latt}$ and Co^{3+}/Co^{2+} surface ratios larger and reducibility and basicity greater than its sheet-like and cube-like counterparts. Accordingly, the Co_3O_4-rod showed the best performance for the formaldehyde total oxidation, the T_{50} temperatures being ranked in the order Co_3O_4-rod < Co_3O_4-sheet < Co_3O_4-cube. Moreover, the Co_3O_4-rod catalyst completely converted formaldehyde at 120 °C, with excellent time on stream stability.

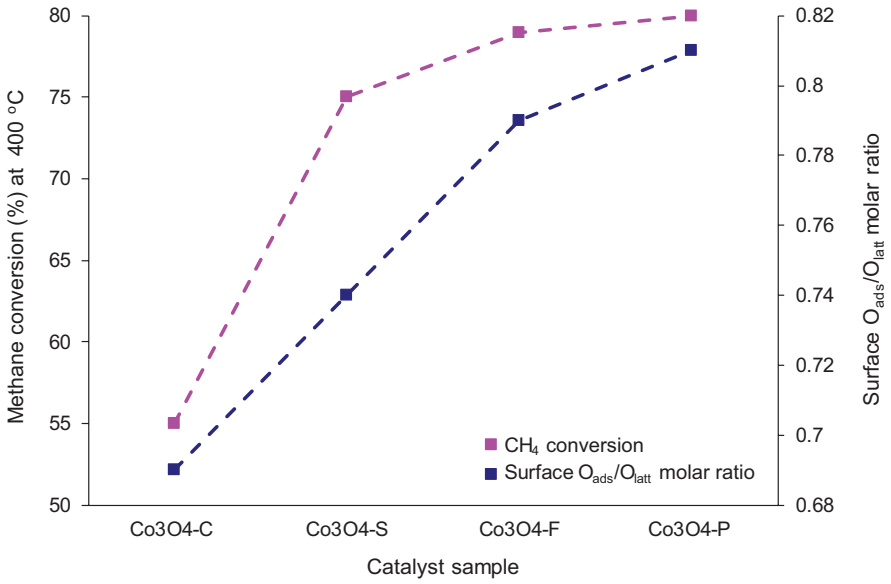

Fig. 1.5 Correlation between the catalytic activity in methane combustion and surface O_{ads}/O_{latt} molar ratio for Co_3O_4 nanocrystals with different morphologies: cubic (C), hexagonal sheet-like (S), flower-like (F), and hexagonal plate-like (P) (Reaction conditions: 0.2 vol. % CH_4 in air; GHSV = 110,000 h^{-1}). (Data from ref. [119])

High surface area ordered Co_3O_4 catalysts have been successfully prepared by a nanocasting route using different mesoporous KIT-6 silica as a hard template and tested in the complete oxidation of propane, as a model of short chain alkane, and toluene, as a model of monoaromatic hydrocarbon [121]. It has been shown that the synthesis parameters, i.e., aging and calcination temperatures, of the silica template strongly influence the physicochemical properties and, hence, catalytic performances of the final catalysts. Thus, siliceous KIT-6 hard templates were prepared at three different aging temperatures (40, 70, and 100 °C) and calcined at 550 °C (denoted KIT6-40–550, KIT6-70–550, and KIT6-100–550, respectively). Additionally, the silica sample aged at 100 °C was calcined at 700, 800, and 900 °C (samples KIT6-100–700, KIT6-100–800, and KIT6-100–900, respectively). They were impregnated with the Co-precursor (Co nitrate), then calcined at 550 °C for 6 h, and finally the silica template was eliminated using a concentrated aqueous solution of NaOH to obtain the corresponding mesoporous cobalt oxides C40–550, C70–550, C100–550, C100–700, C100–800, and C100–900, respectively. These catalytic materials were shown to be more active in the total oxidation reaction compared with a conventional Co_3O_4 prepared by simple evaporation of cobalt nitrate followed by calcination. The best C100–550 catalyst showed T_{50} temperatures (corresponding to 50% conversion) of 196 and 164 °C in propane and toluene combustion, respectively, which are significantly lower compared to the conventional Co_3O_4 (235 °C and 260 °C, respectively) (Fig. 1.6). Interestingly, an inverse

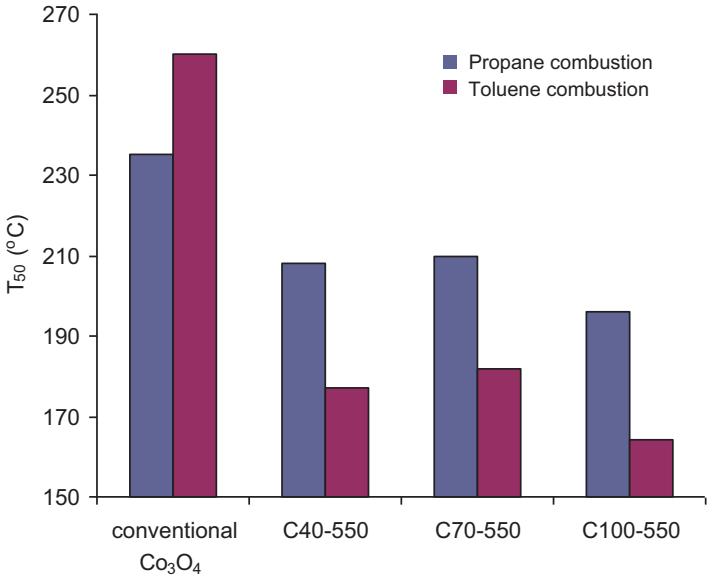

Fig. 1.6 Influence of the aging temperature during the synthesis of the silica template (40, 70, and 100 °C) on the catalytic activity of the corresponding mesoporous Co_3O_4 catalysts (expressed as T_{50}) in complete oxidation of propane and toluene and comparison with Co_3O_4 prepared by simple evaporation of Co nitrate (Reaction conditions: 8000 ppm C_3H_8 in air; GHSV = 12,000 mL g_{cat}^{-1} h^{-1} and 100 ppm C_7H_8 in air; GHSV = 60,000 mL g_{cat}^{-1} h^{-1}, respectively). (Data from ref. [121])

relationship between the ordered structure of these catalysts and their activity was found. For example, the C100–550 catalyst, which possesses a partly ordered structure, leads to a higher conversion per surface area in propane combustion than the C40–550 sample which has a highly ordered, bimodal structure. Since the reducibility was not very different among ordered and non-ordered catalysts, it was concluded that the enhanced activity of the non- or partly ordered catalysts is due to a higher concentration of highly reactive oxygen defects (a higher concentration of surface Co^{2+} species) in these materials. Notably, it has been shown that these catalysts exhibit high stability at moderate temperatures, regardless of the test molecule.

Ordered mesoporous Co_3O_4 spinel prepared by the nano-replication method using either SBA-15 (Co_3O_4-S) or KIT-6 (Co_3O_4-K) templates was studied in the catalytic oxidation of dibromomethane (CH_2Br_2) as a model pollutant for Br-VOC [122]. The ordered mesoporous spinel samples were shown to be the replica structures of their templates with unimodal pore size distribution centered at 3.9 and 3.6 nm for Co_3O_4-S and Co_3O_4-K, respectively, and have lower crystallinity and smaller crystallite size compared with a precipitated counterpart (Co_3O_4-B). Also, the ordered mesoporous spinel samples have significantly larger surface areas and better redox properties compared to that of Co_3O_4-B. Both the Co^{3+}/Co^{2+} surface ratio and the ratio of the surface-adsorbed oxygen to lattice oxygen (O_{ads}/O_{latt}) increased following the order: Co_3O_4-B < Co_3O_4-S < Co_3O_4-K. In the same order,

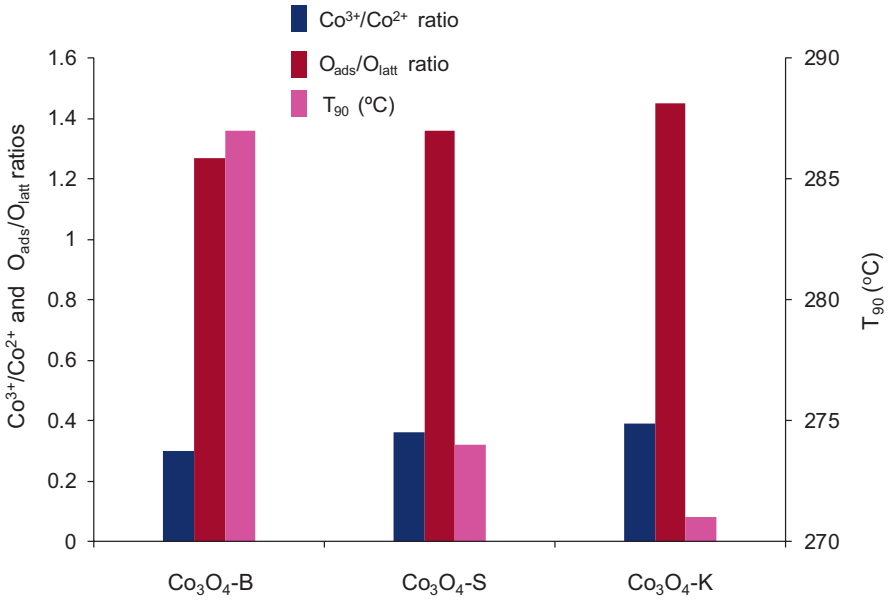

Fig. 1.7 Catalytic activity (in terms of T_{90} values) in the oxidation of CH_2Br_2 and Co^{3+}/Co^{2+} and O_{ads}/O_{latt} ratios for the different Co_3O_4 materials (Reaction conditions: 500 ppm CH_2Br_2, 10% O_2 and balancing N_2; GHSV = 112,500 $cm^3\ g_{cat}^{-1}\ h^{-1}$). (Data from ref. [122])

their catalytic performance oxidation reaction of CH_2Br_2 increased. The superior catalytic activity of ordered mesoporous spinel catalysts was attributed to their high specific surface areas and strong redox property together with their higher content of superficial Co^{3+} species and surface active oxygen (Fig. 1.7). Notably, the most active catalyst in this series, i.e., Co_3O_4-K, also showed the highest selectivity to CO_2 at low temperature and a good time-on-stream stability for at least 30 h.

A series of Co_3O_4 catalysts were synthesized at different pH values by a facile precipitation method, the influence of preparation pH on the catalytic performance in methane combustion being investigated [123]. The final catalysts were denoted as Co_3O_4-*X*, where *X* (8.0; 8.5; 9.0; 9.5; 10) represents the pH values at the end point of titration, which strongly influenced their physicochemical characteristics and, hence, their catalytic performance. Indeed, their surface area passes through a minimum (25.2 $m^2\ g^{-1}$) and the crystallite size through a maximum (33.4 nm) for Co_3O_4-9.0 sample, which also shows maxima of surface Co^{2+}/Co^{3+} (0.46) and O_{ads}/O_{latt} (0.51) ratios. Notably, the catalytic activity of the Co_3O_4-*X* samples in terms of intrinsic reaction rate passes through a maximum for Co_3O_4-9.0 and correlates well with the surface Co^{2+}/Co^{3+} and O_{ads}/O_{latt} ratios (Fig. 1.8). Co_3O_4-9.0 catalyst also shows the lowest T_{50} and T_{90} temperatures (corresponding to 50 and 90% methane conversion, respectively), i.e., 344 °C and 413 °C, respectively, and possesses good long-term stability, no loss of catalytic activity being recorded after 60 h on stream.

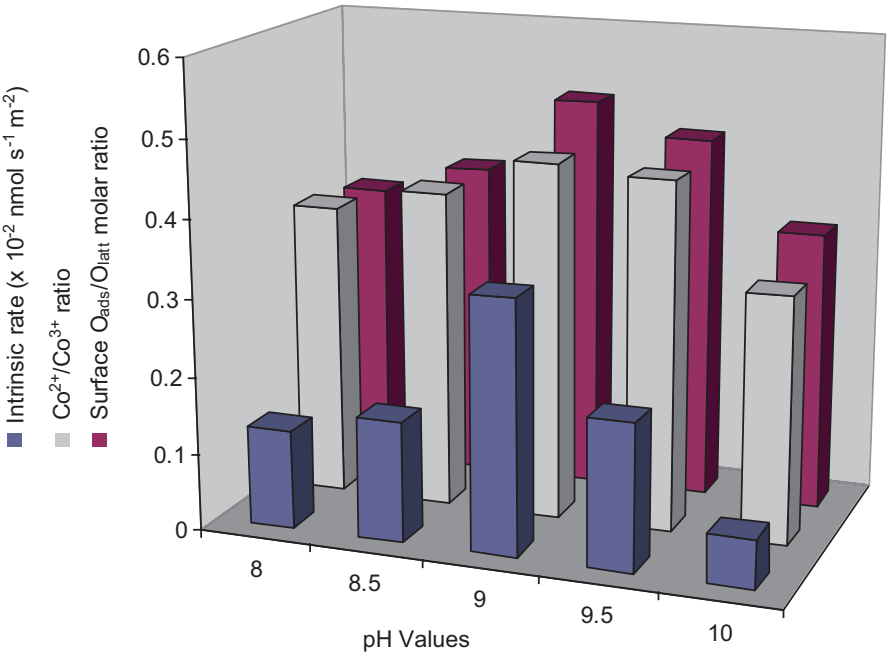

Fig. 1.8 Influence of preparation pH on the surface Co^{2+}/Co^{3+} and O_{ads}/O_{latt} ratios of Co_3O_4-*X* catalysts and on their activity in methane combustion (Reaction conditions: 0.5 vol. % CH_4, 8 vol. % O_2 and balancing N_2; GHSV = 18,000 mL g_{cat}^{-1} h^{-1}). (Data from ref. [123])

A nanosized Co_3O_4 catalyst for the complete oxidation of propane and CO was prepared by dispersion-precipitation (DP) [124]. Compared with the conventional alkali-induced precipitation (AP) method, this method involves the reaction between wet cobalt hydroxide and acetic acid, with the formation of a colloidal dispersion, followed by a subsequent dilution which destabilizes and precipitates the colloidal particles. The oxide thus obtained (CoDP) had smaller particle size, lower crystallinity, higher surface area, and larger pore volume compared to its conventionally precipitated counterpart (CoAP). Moreover, CoDP was shown to be more reducible and to possess larger amount of reactive surface-adsorbed oxygen species. These superior properties of CoDP make it a significantly better catalyst than CoAP for the complete oxidation of both C_3H_8 and CO. Thus, C_3H_8 was completely oxidized on CoDP catalyst at 240 °C, whereas only ca. 21% conversion was achieved on CoAP, even at 300 °C. Regarding the catalytic oxidation of CO, complete conversion was achieved at ca. 110 °C on CoDP catalyst and at ca. 170 °C on CoAP. Notably, CoDP catalyst showed a good long-term stability in the total oxidation of propane.

Three different methods, i.e., nonequilibrium plasma deposition (NEP), Langmuir-Blodgett (LB), and impregnation, were used to prepare a series of cobalt oxide catalysts deposited on precalcined metallic carriers with two different geometries, i.e., wire gauze and sheets, in order to compare the efficiency of deposition,

the chemical properties of the catalyst, and its catalytic performance in n-hexane combustion [125]. First, it is worth describing shortly the principles of NEP and LB methods, which are less usual for the preparation of catalytic materials. The NEP technique is used to obtain thin-film materials deposited on various carriers, starting from metal-organic precursors in a plasma reactor operated at low pressure [126–128]. Thus, the metal-organic precursor is transported with a carrier gas (argon and/or oxygen) through the region of low temperature nonequilibrium plasma of an electric discharge where its decomposition/oxidation takes place followed by the deposition of the metal or metal oxide on the support material [126–128]. Usually, precalcined Cr-Al stainless steel leaves, steel wire gauzes, kanthal steel, and steel sheets are used as support materials, while cyclopentadienyldicarbonyl-cobalt (I), Cu(II)-acetylacetate, etc. are examples of metal-organic precursors [127–129]. The LB deposition is a technique used to prepare highly ordered, defectless film layers of controlled thickness and architecture of a compound on a solid surface [130, 131]. In this method, a single layer of molecules is initially organized on a liquid surface, usually water, before being transferred onto a solid support to form a thin film having the thickness of a constituent molecule. If the process is repeated, multilayered films can be obtained [130, 132]. Although the method requires a sophisticated equipment (Langmuir trough), it allows permanent control of the several physical parameters of layers transferred, such as molecular packing, composition, and quantity [130–132]. Among the catalyst layering methods used to prepare deposited cobalt oxide catalysts, the NEP technique was found to be the most adequate for the deposition of materials on the structural reactors for catalytic applications, since it allows the control of the dispersion of the deposited material, maintaining at the same time the geometry of the carriers [125]. Contrarily, in the case of LB method, the deposition efficiency was too low to obtain an active catalyst within reasonable time, while the impregnation method did not allow the control of the thickness of the deposited layers [125]. The NEP layering method led to a well-dispersed cobalt oxide catalyst with spinel structure, which turned out to be only slightly less active than the commercial Pt catalyst in *n*-hexane combustion [125].

A series of structured cobalt spinel catalysts prepared by NEP deposition of thin films on precalcined metallic supports (kanthal sheets) was studied in *n*-nonane catalytic combustion reaction [133]. The different catalysts were prepared under different atmospheres (oxygen-free and oxygen/argon) and residence times of the precursor (Co(I)-cyclopentadienyldicarbonyl) in the plasma reactor. This induced significant changes in the catalysts' structure and morphology, including the amount and the shape of the particles deposited on the metallic support. The catalytic tests showed that the most active systems in the *n*-nonane combustion reaction are the samples synthesized under oxygenless conditions. Contrarily, the activity is significantly lower for the catalysts prepared under synthetic air conditions for which the dominant form of the cobalt oxide is its amorphous phase highly dispersed on alumina.

Incipient wetness impregnation (IWI) and a combination of IWI and subsequent combustion synthesis (CS) were used to prepare a series of $Co_3O_4/\gamma\text{-}Al_2O_3$ catalysts with different Co_3O_4 loadings, tested in the catalytic combustion of CH_4 [134]. The

IWI method consisted of dripping an aqueous solution of cobalt nitrate onto γ-Al_2O_3 followed by water evaporation, drying, and calcination at 700 °C in air, while for the IWI/CS method, the impregnation was realized with aqueous solutions of cobalt nitrate and urea (molar ratio = 2:1), then the dried sample was heated to initiate the exothermic reactions at 230–250 °C for 5 min. The self-propagating flameless combustion led to the complete IWI/CS catalyst formation within 1–15 min. It has been shown that the IWI/CS-X catalysts (*X* = 5, 10, 30, and 50, representing the Co_3O_4 loading as wt %) have lower degree of crystallization, smaller average crystallite size, greater surface area, and higher degree of dispersion of Co_3O_4 on the γ-Al_2O_3 support, in comparison with the IWI-X catalysts with similar Co_3O_4 content. The large quantities of vapors (e.g., CO_2, H_2O, and NO_2) rapidly released in the combustion process, which is completed in a very short time, limit the growth of spinel crystals. Moreover, for the IWI/CS-X catalysts, the synthesis process determined the formation of abundant easily reducible surface Co^{3+} species. Accordingly, the IWI/CS-X catalysts have excellent catalytic performance in CH_4 combustion, being significantly more active than their IWI-X counterparts (Fig. 1.9). In particular, IWI/CS-30 catalyst, which possesses the smallest average particle size (6.5 nm) and the highest surface $Co^{3+}/(Co^{2+}+Co^{3+})$ ratio, exhibited the best catalytic activity with total conversion of CH_4 achieved at 550 °C. On the other hand, the excessive loading of Co_3O_4 in IWI/CS-50 sample led to a diminished catalytic activity.

A series of nanoflower-like nickel foam monolith-supported Co_3O_4 catalysts, prepared via a green and facile electrodeposition method, was studied in the propane total oxidation [135]. The amount and interaction of Co_3O_4 loaded on the

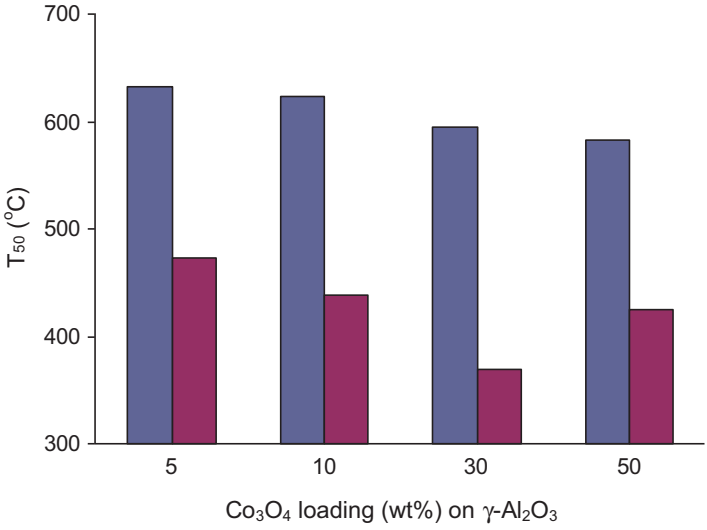

Fig. 1.9 Comparison between T_{50} temperatures in CH_4 combustion on catalysts with similar Co_3O_4 loadings prepared via two methods: IWI (■) and IWI/CS (■) (Reaction conditions: 0.2 vol % CH_4, 10 vol % O_2, and N_2 as the balance gas; GHSV = 36,000 mL g_{cat}^{-1} h^{-1}). (Data from ref. [134])

Ni-foam monolith were controlled by the time duration of potential deposition. The resulted catalysts were denoted as Co-NF-*t*, where *t* represents the corresponding electrodeposition time duration in seconds, i.e., Co-NF-300, Co-NF-600, Co-NF-900, and Co-NF-3600. For comparison, a pure Co_3O_4 catalyst was also synthesized by thermal decomposition of cobalt nitrate, using the same calcination conditions. For example, it has been shown that Co-NF-300 nanosheet (diameter 1–2 μm) stacked by Co_3O_4 nanoparticles (10–30 nm) presents an abundance of pores. Such 3D hierarchical microstructures with interconnected pore channels expose more active sites (larger cobalt oxide surface), without any reactant/product diffusion limitations. All of the Co-NF-*t* are flower-like sheets with the same morphology and microstructure, the electrodeposition time duration having no obvious effect on these characteristics. On the other hand, the morphology of pure Co_3O_4 is different from that of Co-NF-*t*, its shape being elongated and particle size significantly larger (10–50 nm). Co_3O_4 loading and the intensity of the diffraction lines corresponding to Co_3O_4 with spinel structure increased with the deposition time duration. The spinel particle size for the Co-NF-*t* is small and varies between 18 and 21 nm. Strong interactions between Co_3O_4 and Ni-foams were shown to be formed during the electrodeposition process, enhancing the reducibility of Co_3O_4. The $Co^{2+}/(Co^{2+} + Co^{3+})$ ratio calculated from the areas of reduction peaks appears to depend strongly on the deposition time duration, Co_3O_4 supported on Ni-foam having

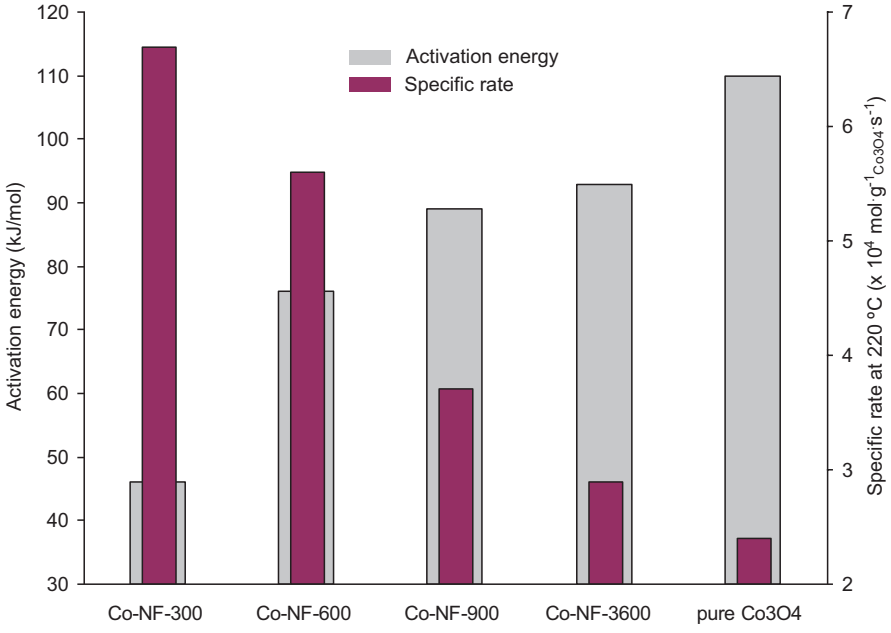

Fig. 1.10 Variation of the specific reaction rates (per gram of Co_3O_4) at 220 °C and of the activation energies for the Co-NF-*t* catalysts in comparison with pure Co_3O_4 (Reaction conditions: 1000 ppm C_3H_8 in air; GHSV = 30,000 mL g_{cat}^{-1} h^{-1}). (Data from ref. [135])

higher Co^{2+} content compared with pure Co_3O_4 sample. Both the Co^{2+} content and catalytic activity increase in the order: pure Co_3O_4 < Co-NF-3600 < Co-NF-900 < Co-NF-600 < Co-NF-300. With the highest specific activity and the lowest activation energy, Co-NF-300 sample was found to be the most active in total oxidation of propane reaction (Fig. 1.10). Moreover, Co-NF-300 sample also possesses good time on stream stability for 40 h of reaction.

To separately study the geometrical-site-dependent catalytic activity of tetrahedrally coordinated Co^{2+} sites (Co^{2+}_{Td}), octahedrally coordinated Co^{2+} sites (Co^{2+}_{Oh}), and octahedrally coordinated Co^{3+} sites (Co^{3+}_{Oh}) in VOC oxidation, a series of Co-based catalysts, i.e., Co_3O_4, CoO, $CoAl_2O_4$, $ZnCo_2O_4$, and $CoFe_2O_4$, was prepared by the nanocasting method using mesoporous silica KIT-6 as a hard template [3]. Thus, starting from three-dimensionally ordered mesoporous Co_3O_4, Co^{2+} or Co^{3+} sites were replaced with catalytically inactive or less active Zn^{2+} (d^0), Al^{3+} (d^0), and Fe^{3+} (d^5), respectively. It has been shown that not only Co^{3+}_{Oh} species act as active sites, but also Co^{2+}_{Oh} sites exhibit high catalytic activity due to the fact that they are easily oxidized to active Co^{3+} species which were shown to be responsible for the formation of carboxylate species, the main intermediate in the oxidation of benzene. Therefore, $ZnCo_2O_4$ with Co^{3+}_{Oh} and CoO with Co^{2+}_{Oh} species exhibit good catalytic activity in benzene oxidation and high TOF_{Co} values at low temperature. Moreover, $ZnCo_2O_4$ exhibits good durability at 500 °C and strong water resistance ability. Contrarily, $CoAl_2O_4$ with Co^{2+}_{Td} sites show poor catalytic activity and a low TOF_{Co} value.

1.4.2 M-Co Spinels (M = Transition Metal)

A series of ordered mesoporous MCo_2O_4 (M = Cu, Zn, and Ni) spinel catalysts, synthesized via nano-replication method using mesoporous silica KIT-6 as a hard template, was tested in the complete oxidation of methane reaction and compared with bulk MCo_2O_4 spinel catalysts prepared by coprecipitation [136]. The ordered structure of mesoporous MCo_2O_4 (m-MCo_2O_4) spinel catalysts was clearly confirmed by the combined results of N_2 adsorption-desorption and TEM and XRD analysis. Indeed, the N_2 adsorption-desorption measurements revealed that all the m-MCo_2O_4 samples show a type IV isotherm with H1 hysteresis loop and a narrow pore size distribution, confirming the formation of mesoporous structure responsible for their higher surface area and pore volume than their bulk counterpart (b-MCo_2O_4). Also, TEM analysis clearly suggests that m-MCo_2O_4 spinels are well-replicated from the KIT-6 template, their wall thickness corresponding well with the pore size diameter of KIT-6 template. Moreover, the low angle XRD patterns prove the formation of ordered mesoporous structures of the m-MCo_2O_4 spinels, in line with the results of N_2 adsorption-desorption and TEM analysis. At the same time, wide angle XRD analysis shows that m-MCo_2O_4 spinels possess smaller size of crystallites than b-MCo_2O_4 spinels, which leads to greater resistance to decomposition and higher resistance to sintering during calcination of the spinel phase. XPS

analysis revealed that the normalized amount of Co^{3+} cations on the surface decreases for m-MCo_2O_4 spinels as follows: m-$CuCo_2O_4$ > m-$ZnCo_2O_4$ > m-$NiCo_2O_4$. The catalytic activity of the meso catalysts in methane combustion, expressed as T_{50} and T_{90} temperatures (corresponding to 50% and 90% conversion, respectively), is considerably lower than that of their bulk counterpart, obviously due to the unique ordered mesostructure and the excellent thermal stability of the former. Notably, the activity of the meso catalysts increases with increasing the normalized amount of surface Co^{3+} cations (Fig. 1.11), clearly suggesting that they play a key role in improving the catalytic activity.

A series of spinel MCo_2O_4 (M = Co, Ni, Cu) hollow mesoporous spheres (HMS) was prepared by solvothermal alcoholysis, in order to induce a cation-substituting effect on Co_3O_4 spinel with the aim of improving the activity in total oxidation of VOC [137]. The cubic spinel was the main phase present in all the catalysts, with tiny amounts of NiO and CuO side phases in NiHMS and CuHMS, respectively. It has been shown that the number of the defective sites determined by Raman spectroscopy, the surface O_{ads}/O_{latt} and Co^{3+}/Co^{2+} molar ratios, and the catalyst reducibility, both in terms of hydrogen consumption and easiness of reduction, increased in the following order: CoHMS < NiHMS < CuHMS. Accordingly, the activity in

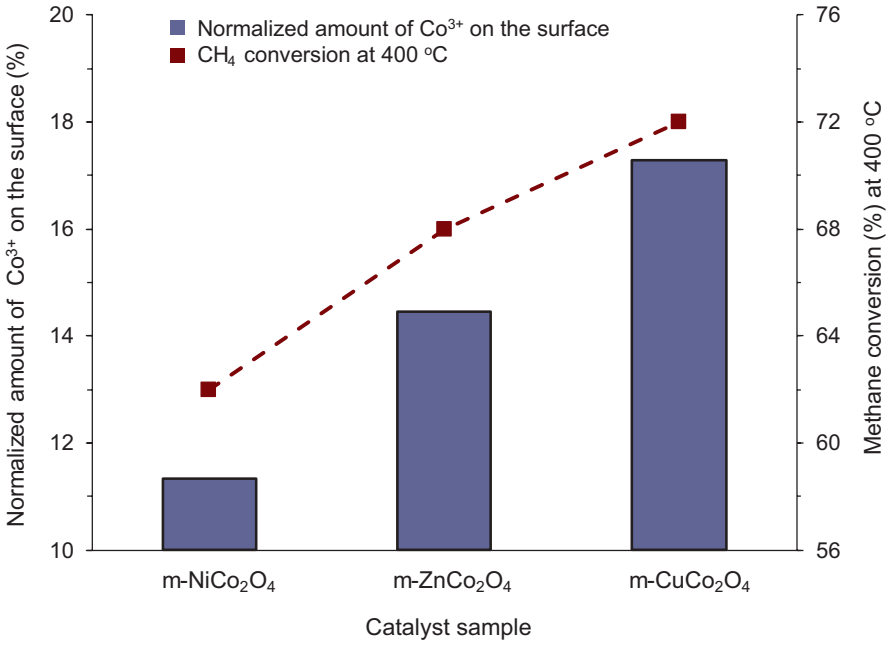

Fig. 1.11 Correlation between the catalytic activity in methane combustion and the normalized amount of Co^{3+} cations on the surface of m-$NiCo_2O_4$, m-$ZnCo_2O_4$, and m-$CuCo_2O_4$ spinel catalysts (Reaction conditions: 1500 ppm CH_4, 12.12 vol. % O_2 and balancing N_2, total flow rate of 200 mL min^{-1}, GHSV = 60,000 mL g_{cat}^{-1} h^{-1}). (Data from ref. [136])

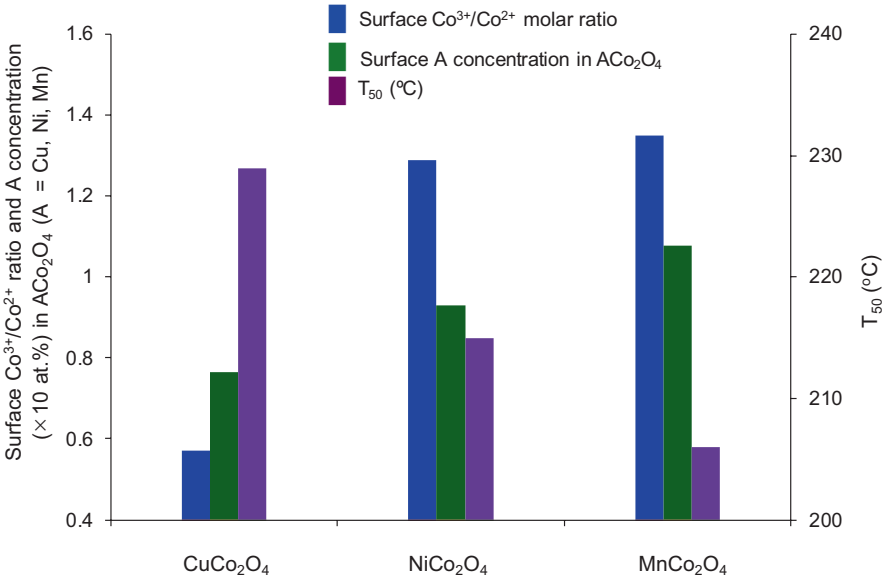

Fig. 1.12 Co^{3+}/Co^{2+} surface ratio and the surface concentration of A cation in ACo_2O_4 (A = Cu, Ni, Mn) catalysts and their activity (in terms of T_{50} values) in the complete oxidation of benzene (Reaction conditions: 1000 ppm C_6H_6 in air; GHSV = 90,000 mL g_{cat}^{-1} h^{-1}). (Data from ref. [118])

the total oxidation of acetone as model VOC followed the same order. The most active catalyst, CuHMS, also showed long-term stability and good water tolerance.

Nanocrystalline ordered mesoporous ACo_2O_4 (A = Cu, Ni and Mn) catalysts prepared by a simple co-nanocasting method using SBA-15 as a hard template were studied in benzene total oxidation reaction [118]. It has been shown that both the surface A content and Co^{3+}/Co^{2+} molar ratio in ACo_2O_4 decrease as follows: $MnCo_2O_4$ > $NiCo_2O_4$ > $CuCo_2O_4$. These characteristics were correlated with the catalytic performance in benzene total oxidation (Fig. 1.12), $MnCo_2O_4$ being the best catalyst in this series. Moreover, it showed high thermal stability and good tolerance against water vapor. It is worth noting that the oxidation of benzene over these ACo_2O_4 catalysts involves both the Mars-van Krevelen and Langmuir-Hinshelwood mechanisms [118].

A series of $ZrO_2(x)$-Co_3O_4 mixed oxide catalysts with x = 0; 0.5; 2; 5; 8; and 10 wt. % and forming a solid solution with the spinel structure was prepared by coprecipitation and tested in the catalytic combustion of lean methane at low temperature [138]. Their BET surface area increases monotonous with increasing ZrO_2 content, while the crystallite size decreases. The surface O_{ads}/O_{latt} molar ratio increased with increasing ZrO_2 content from 0 to 2% and then decreased with further increasing ZrO_2. This is consistent with the variation of the catalytic activity in methane combustion which passes through a maximum for 2 wt % ZrO_2 (Fig. 1.13). Similarly, the surface ratio between the Co^{2+} in tetrahedral coordination and Co^{3+} in octahedral coordination passes through a maximum for the $ZrO_2(x)$-Co_3O_4 system

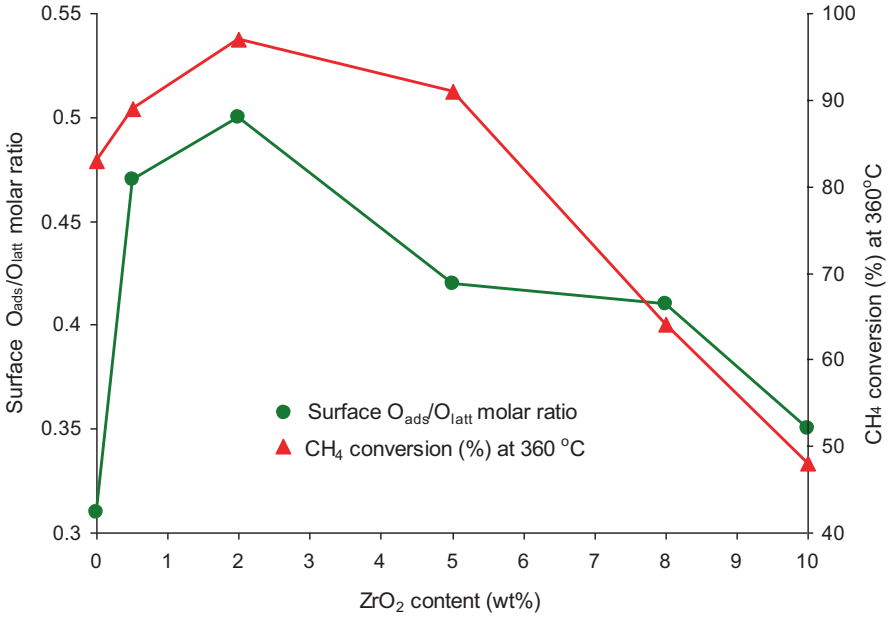

Fig. 1.13 Variation of surface O_{ads}/O_{latt} molar ratio and of the catalytic activity in methane combustion as a function of ZrO_2 content in $ZrO_2(x)$-Co_3O_4 catalysts (Reaction conditions: 0.5% CH_4, 8.0% O_2, 91.5% N_2; GHSV = 12,000 mL g_{cat}^{-1} h^{-1}). (Data from ref. [138])

with $x = 2\%$, suggesting that the Co^{2+} tetrahedral sites also play an important role in methane combustion (Fig. 1.14). Notably, no deactivation phenomenon was observed during the catalytic tests, proving the superior stability of these catalysts.

A series of Cu-containing mixed oxides with spinel structure, i.e., $CuCo_2O_4$, $CuMn_2O_4$, and $CuCr_2O_4$, prepared by a sol-gel combustion method, was studied in the catalytic oxidation of 2-propanol as a model molecule of oxygenated VOC [139]. Cu-Cr mixed oxide was pure $CuCr_2O_4$ spinel, while Cu-Mn and Cu-Co mixed oxides consisted of mixtures of spinel and copper oxide phases. The catalysts containing both spinel and CuO phases, i.e., Cu-Mn and Cu-Co mixed oxides, were shown to be more active than the pure $CuCr_2O_4$ spinel. This behavior was attributed to a synergistic cooperation between CuO and spinel phases which enhances the catalytic performance.

The different Co-based spinel catalysts hereby described, their preparation methods, and their catalytic applications together with the best performance are summarized in Table 1.3.

The main conclusion of the analysis presented above is that the most important factors controlling the catalytic performance of Co-based spinels in the complete oxidation reaction of VOC are the Co^{3+}/Co^{2+} surface mol ratio and the ratio of the surface-adsorbed oxygen to lattice oxygen. They are influenced by the method of preparation used, including the procedure and conditions adopted for a given

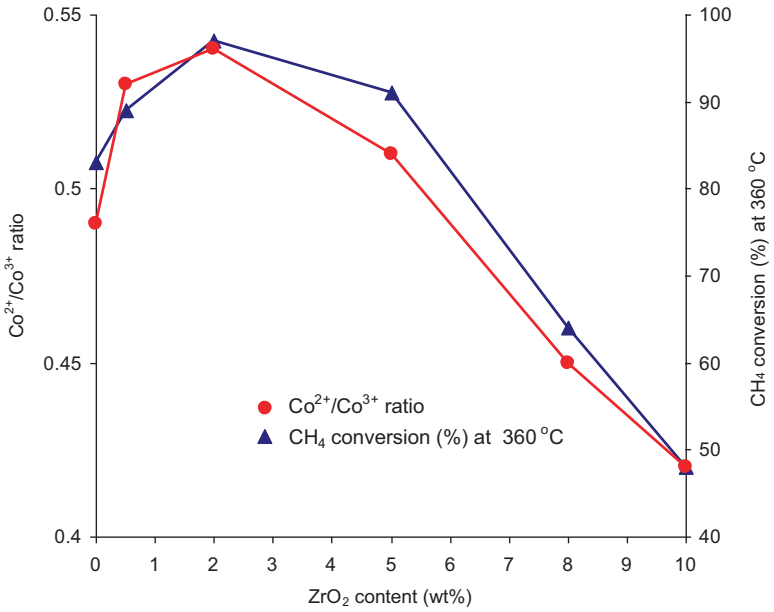

Fig. 1.14 Variation of Co^{2+}/Co^{3+} surface ratio and of the catalytic activity in methane combustion as a function of ZrO_2 content in $ZrO_2(x)$-Co_3O_4 catalysts (Reaction conditions: 0.5% CH_4, 8.0% O_2, 91.5% N_2; GHSV = 12,000 mL g_{cat}^{-1} h^{-1}). (Data from ref. [138])

method, and by the nature and surface concentration of cation M in MCo_2O_4 cobaltites.

1.5 General Conclusion

Fe-, Mn-, and Co-based spinel oxides catalysts show high catalytic performances, including stability on stream, for the total oxidation of a wide range of VOC, and some of them were shown to have activities close to that of the noble metal catalysts. Their catalytic properties are complex functions of their bulk and surface characteristics which are determined by their composition and preparation method. Indeed, the method of preparation used to synthesize the spinel oxides and, for a given method, the nature of the starting materials and reagents, the pH, the aging conditions as well as the thermal treatment of the catalyst precursors and the post-synthesis modification strongly influence their phase purity and homogeneity, textural properties, particle size and morphology, cation distribution in the spinel structure, density of surface defects and reduction ability and, hence, their catalytic performance. Also, the redox and electronic properties of the spinels, which are key factors controlling their activity in total oxidation reaction, can be tuned by varying their chemical composition. Indeed, the nature of both cations A and M in AM_2O_4

Table 1.3 Preparation and catalytic performance of the cobaltite spinel catalysts in VOC total oxidation

Catalysts	Preparation Method	Tested chemical compound (reaction conditions)	Best results	Ref.
Co_3O_4 nanocrystals with different morphologies	HT[h] method	Methane (0.2 vol. % CH_4 in air; GHSV = 110,000 h^{-1})	T_{50} = 346 °C on Co_3O_4 with flower-like morphology	[119]
Co_3O_4 with different morphologies	Modified PP[b]/HT[h]	Formic aldehyde (100 ppm HCHO, 21 vol. % O_2 and balancing N_2; GHSV = 69,000 h^{-1})	T_{50} = 72 °C on Co_3O_4 with rod-like morphology	[120]
Nano-replicated ordered Co_3O_4 on KIT-6 hard templates synthesized at different aging and calcination temperatures	NR[c] using mesoporous silica KIT-6	Propane (8000 ppm C_3H_8 in air; GHSV = 12,000 mL g_{cat}^{-1} h^{-1}) Toluene (100 ppm C_7H_8 in air; GHSV = 60,000 mL g_{cat}^{-1} h^{-1})	T_{50} = 196 and 164 °C for propane and toluene, respectively, on Co_3O_4 replicated on KIT-6 aged and calcined at 100 °C and 550 °C, respectively	[121]
Ordered mesoporous Co_3O_4/bulk Co_3O_4	NR[c] using SBA-15 or KIT-6/CoPP[d]	Dibromomethane (500 ppm CH_2Br_2, 10% O_2 and balancing N_2; GHSV = 112,500 cm^3 g_{cat}^{-1} h^{-1})	T_{50} = 235 °C on Co_3O_4-K (synthesized using KIT-6 template)	[122]
Co_3O_4	PP[b] at different pH values	Methane (0.5 vol. % CH_4, 8 vol. % O_2 and balancing N_2; GHSV = 18,000 mL g_{cat}^{-1} h^{-1})	T_{50} = 344 °C on Co_3O_4-9.0 (synthesized at pH = 9.0)	[123]
Nanosized Co_3O_4 catalysts	DP[e]/conventional PP[b]	Propane (1000 ppm C_3H_8 in air; GHSV = 24,000 h^{-1}) CO (10,000 ppm CO in air; GHSV = 12,000 h^{-1})	T_{50} = 194 and 83 °C for propane and CO, respectively, on nanosized Co_3O_4 prepared by DP	[124]
Co_3O_4 deposited on wire gauze and metallic sheets carriers	NEP[f], LB[g], and IMP[h]	*n*-hexane (0.75 mol. % C_6H_{14} in air; Total flow = 100 mL min^{-1})	Best results obtained on Co_3O_4 deposited by NEP on wire gauze carrier	[125]
Structured cobalt catalysts, deposited on metallic supports	NEP[f] under different conditions	*n*-nonane (2000 ppm C_9H_{20}, 20 vol. % O_2 and balancing He; Total flow = 25 mL min^{-1})	T_{50} = 320 °C on the catalyst prepared under oxygen-free conditions, with the highest value of the monomer flow	[133]
Co_3O_4/γ-Al_2O_3 with different Co_3O_4 loadings (5, 10, 30, and 50 wt%)	IWI[i] and a combination of IWI and CS[j]	Methane (0.2 vol. % CH_4, 10 vol. % O_2, and balancing N_2; GHSV = 36,000 mL g_{cat}^{-1} h^{-1})	T_{50} = 371 °C on Co_3O_4/γ-Al_2O_3 with 30 wt% Co_3O_4 prepared by IWI/CS	[134]
Nanoflower-like nickel foam-supported Co_3O_4 monolith	In situ ED[k] using different deposition times	Propane (1000 ppm C_3H_8 in air; GHSV = 30,000 mL g_{cat}^{-1} h^{-1})	Best results obtained on Co-NF-300 s (deposition time = 300 s)	[135]

(continued)

Table 1.3 (continued)

Catalysts	Preparation Method	Tested chemical compound (reaction conditions)	Best results	Ref.
Co_3O_4, CoO, $CoAl_2O_4$, $ZnCo_2O_4$, and $CoFe_2O_4$	NC[l] using mesoporous silica KIT-6	Benzene (498 ppm C_6H_6, 20 vol. % O_2 and balancing N_2; GHSV = 90,000 mL g_{cat}^{-1} h^{-1})	T_{50} = 196 °C on CoO	[3]
Mesoporous M cobaltite (M = Cu, Zn, and Ni)	NR[c] using mesoporous silica KIT-6	Methane (1500 ppm CH_4, 12.12 vol. % O_2 and balancing N_2; GHSV = 60,000 mL g_{cat}^{-1} h^{-1})	T_{50} = 369 °C on mesoporous $CuCo_2O_4$	[136]
M cobaltite (M = Co, Ni, Cu) hollow mesoporous spheres (HMS)	Solvothermal alcoholysis	Acetone (1000 ppm acetone, 20% O_2 and balancing N_2; WHSV = 93,000 mL g_{cat}^{-1} h^{-1})	T_{50} = 157 °C on $CuCo_2O_4$ (CuHSM)	[137]
Mesoporous ACo_2O_4 (A = Cu, Ni, and Mn)	NR[c] using SBA-15	Benzene (1000 ppm C_6H_6 in air; GHSV = 90,000 mL g_{cat}^{-1} h^{-1})	T_{50} = 206 °C on $MnCo_2O_4$	[118]
$ZrO_2(x)$-Co_3O_4 (x = 0; 0.5; 2; 5; 8; and 10 wt.%)	CoPP[d]	Methane (0.5% CH_4, 8.0% O_2, 91.5% N_2; GHSV = 12,000 mL g_{cat}^{-1} h^{-1})	T_{50} = 279 °C on $ZrO_2(2)$-Co_3O_4	[138]
Cu cobaltite, Cu manganite, Cu chromite	SG[m] + SelfC[n]	2-propanol (0.085 mol mol^{-1} C_3H_8O in air; GHSV = 2400 h^{-1})	T_{50} = 150 °C on $CuCo_2O_4$	[139]

[a]*HT* hydrothermal method
[b]*PP* precipitation
[c]*NR* nano-replication
[d]*CoPP* coprecipitation
[e]*DP* dispersion-precipitation
[f]*NEP* nonequilibrium plasma deposition
[g]*LB* Langmuir–Blogett method
[h]*IMP* impregnation
[i]*IWI* incipient wetness impregnation
[j]*CS* combustion synthesis
[k]*ED* electrodeposition
[l]*NC* nanocasting method
[m]*SG* sol-gel method
[n]*SelfC* self-combustion

(M = Fe, Mn and Co) binary spinels and the addition of a third cation, which can lead to a ternary spinel or to phase separation as a function of its ionic size, strongly influence the catalytic behavior due to synergistic effects between the different cations or phases rationalized on the basis of enhanced electron transfer and oxygen nonstoichiometry.

Finally, through the presented examples, this chapter clearly demonstrates the high potential of Fe-, Mn-, and Co-based spinels as total oxidation catalysts for VOC.

References

1. C. He, J. Cheng, X. Zhang, M. Douthwaite, S. Pattisson, Z. Hao, Recent advances in the catalytic oxidation of volatile organic compounds: a review based on pollutant sorts and sources. Chem. Rev. **119**, 4471–4568 (2019). https://doi.org/10.1021/acs.chemrev.8b00408
2. P. Kuśtrowski, A. Rokicińska, T. Kondratowicz, Abatement of volatile organic compounds emission as a target for various human activities including energy production. Adv. Inorg. Chem. **72**, 385–419 (2018). https://doi.org/10.1016/bs.adioch.2018.05.004
3. X. Wang, Y. Liu, T. Zhang, Y. Luo, Z. Lan, K. Zhang, J. Zuo, L. Jiang, R. Wang, Geometrical-site-dependent catalytic activity of ordered mesoporous Co-based spinel for benzene oxidation: in situ DRIFTS study coupled with Raman and XAFS spectroscopy. ACS Catal. **7**, 1626–1636 (2017). https://doi.org/10.1021/acscatal.6b03547
4. M. Răciulete, G. Layrac, F. Papa, C. Negrilă, D. Tichit, I.C. Marcu, Influence of Mn content on the catalytic properties of Cu-(Mn)-Zn-Mg-Al mixed oxides derived from LDH precursors in the total oxidation of methane. Catal. Today **306**, 276–286 (2018). https://doi.org/10.1016/j.cattod.2017.01.013
5. A. Urdă, A. Herraïz, Á. Rédey, I.C. Marcu, Co and Ni ferrospinels as catalysts for propane total oxidation. Catal. Commun. **10**, 1651–1655 (2009). https://doi.org/10.1016/j.catcom.2009.05.002
6. C. Munteanu, M. Caldararu, D. Gingasu, M. Feder, L. Diamandescu, N.I. Ionescu, In situ electrical conductivity and catalytic properties of copper ferrite synthesized by non-conventional methods. Reac. Kinet. Mech. Catal. **104**, 357–368 (2011). https://doi.org/10.1007/s11144-011-0357-5
7. N. Rezlescu, E. Rezlescu, P.D. Popa, C. Doroftei, M. Ignat, Scandium substituted nickel–cobalt ferrite nanoparticles for catalyst applications. Appl. Catal. B Environ. **158-159**, 70–75 (2014). https://doi.org/10.1016/j.apcatb.2014.03.052
8. C. Doroftei, L. Leontie, Synthesis and characterization of some nanostructured composite oxides for low temperature catalytic combustion of dilute propane. RSC Adv. **7**, 27863–27871 (2017). https://doi.org/10.1039/c7ra03916f
9. W.B. Li, J.X. Wang, H. Gong, Catalytic combustion of VOCs on non-noble metal catalysts. Catal. Today **148**, 81–87 (2009). https://doi.org/10.1016/j.cattod.2009.03.007
10. M. Tomatis, H.H. Xu, J. He, X.D. Zhang, Recent development of catalysts for removal of volatile organic compounds in flue gas by combustion: a review. J. Chem. **2016**, 8324826 (2016). https://doi.org/10.1155/2016/8324826
11. M.S. Kamal, S.A. Razzak, M.M. Hossain, Catalytic oxidation of volatile organic compounds (VOCs)—a review. Atmos. Environ. **140**, 117–134 (2016). https://doi.org/10.1016/j.atmosenv.2016.05.031
12. J. Chen, H. Arandiyan, X. Gao, J. Li, Recent advances in catalysts for methane combustion. Catal. Surv. Jpn. **19**, 140–171 (2015). https://doi.org/10.1007/s10563-015-9191-5

13. X.D. Zhang, Y. Wang, Y.Q. Yang, D. Chen, Recent progress in the removal of volatile organic compounds by mesoporous silica materials and supported catalysts. Acta Phys. Chim. Sin. **31**, 1633–1646 (2015). https://doi.org/10.3866/PKU.WHXB201507281
14. Y. Liu, J. Deng, S. Xie, Z. Wang, H. Dai, Catalytic removal of volatile organic compounds using ordered porous transition metal oxide and supported noble metal catalysts. Chin. J. Catal. **37**, 1193–1205 (2016). https://doi.org/10.1016/S1872-2067(16)62457-9
15. Z. Ma, Cobalt oxide catalysts for environmental remediation. Curr. Catal. **3**, 15–26 (2014). https://doi.org/10.2174/22115447113029990017
16. P. Mohapatra, T. Mishra, K.M. Parida, Pillared clay as an effective catalyst for low temperature VOCs decomposition. Key Eng. Mater. **571**, 71–91 (2013). https://doi.org/10.4028/www.scientific.net/KEM.571.71
17. J. Li, M. Hu, S. Zuo, X. Wang, Catalytic combustion of volatile organic compounds on pillared interlayered clay (PILC)-based catalysts. Curr. Opin. Chem. Eng. **20**, 93–98 (2018). https://doi.org/10.1016/j.coche.2018.02.001
18. I.C. Marcu, A. Urdă, I. Popescu, V. Hulea, Layered double hydroxides-based materials as oxidation catalysts (Ch. 3), in *Sustainable Nanosystems Development, Properties and Applications*, ed. by M. V. Putz, M. C. Mirica, (IGI Global, Hershey, PA, 2017), pp. 59–121. https://doi.org/10.4018/978-1-5225-0492-4.ch003
19. A.R. West, *Solid State Chemistry and Its Application*, 2nd edn. (Wiley, 2014), pp. 66–70
20. A. Ahlawat, V.G. Sathe, V.R. Reddy, A. Gupta, Mossbauer, Raman and X-ray diffraction studies of superparamagnetic $NiFe_2O_4$ nanoparticles prepared by sol–gel auto-combustion method. J. Magn. Magn. Mater. **323**, 2049–2054 (2011). https://doi.org/10.1016/j.jmmm.2011.03.017
21. J. Chandradass, A.H. Jadhav, K.H. Kim, H. Kim, Influence of processing methodology on the structural and magnetic behavior of $MgFe_2O_4$ nanopowders. J. Alloys Compd. **517**, 164–169 (2012). https://doi.org/10.1016/j.jallcom.2011.12.071
22. H. Sozeri, Z. Durmus, A. Baykal, Structural and magnetic properties of triethylene glycol stabilized $Zn_xCo_{1-x}Fe_2O_4$ nanoparticles. Mater. Res. Bull. **47**, 2442–2448 (2012). https://doi.org/10.1016/j.materresbull.2012.05.036
23. B.I. Kharisov, H.V. Rasika Dias, O.V. Kharissova, Mini-review: ferrite nanoparticles in the catalysis. Arab. J. Chem. **12**, 1234–1246 (2019). https://doi.org/10.1016/j.arabjc.2014.10.049
24. R.K. Selvan, C.O. Augustin, L.J. Berchmans, R. Saraswathi, Combustion synthesis of $CuFe_2O_4$. Mater. Res. Bull. **38**, 41–54 (2003). https://doi.org/10.1016/S0025-5408(02)01004-8
25. K. Kamala Bharathi, C.V. Ramana, Improved electrical and dielectric properties of La-doped Co ferrite. J. Mater. Res. **26**, 584–591 (2011). https://doi.org/10.1557/jmr.2010.37
26. T. Brylewski, A. Kruk, A. Adamczyk, W. Kucza, M. Stygar, K. Przybylski, Synthesis and characterization of the manganese cobaltite spinel prepared using two "soft chemical" methods. Mater. Chem. Phys. **137**, 310–316 (2012). https://doi.org/10.1016/j.matchemphys.2012.09.026
27. N. Iftimie, E. Rezlescu, P.D. Popa, N. Rezlescu, On the possibility of the use of a nickel ferrite as semiconducting gas sensor. J. Optoelectron. Adv. Mater. **7**, 911–914 (2005)
28. M.A. Valenzuela, P. Bosch, J. Jiménez-Becerrill, O. Quiroz, A.I. Páez, Preparation, characterization and photocatalytic activity of ZnO, Fe_2O_3 and $ZnFe_2O_4$. J. Photochem. Photobiol. A Chem. **148**, 177–182 (2002). https://doi.org/10.1016/S1010-6030(02)00040-0
29. E. Casbeer, V.K. Sharma, X.Z. Li, Synthesis and photocatalytic activity of ferrites under visible light: a review. Sep. Purif. Technol. **87**, 1–14 (2012). https://doi.org/10.1016/j.seppur.2011.11.034
30. P. Guo, G. Zhang, J. Yu, H. Li, X.S. Zhao, Controlled synthesis, magnetic and photocatalytic properties of hollow spheres and colloidal nanocrystal clusters of manganese ferrite. Colloid Surf. A Physicochem. Eng. Asp. **395**, 168–174 (2012). https://doi.org/10.1016/j.colsurfa.2011.12.027

31. M. Su, C. He, V.K. Sharma, M.A. Asi, D. Xia, X. Li, H. Deng, Y. Xiong, Mesoporous zinc ferrite: Synthesis, characterization, and photocatalytic activity with H_2O_2/visible light. J. Hazard. Mater. **211–212**, 95–103 (2012). https://doi.org/10.1016/j.jhazmat.2011.10.006
32. R. Voda, A. Negrea, L. Lupa, M. Ciopec, P. Negrea, C.M. Davidescu, M. Butnariu, Nanocrystalline ferrites used as adsorbent in the treatment process of waste waters resulted from ink jet cartridges manufacturing. Open Chem. **13**, 743–747 (2015). https://doi.org/10.1515/chem-2015-0092
33. K.K. Kefeni, B.B. Mamba, T.A.M. Msagati, Application of spinel ferrite nanoparticles in water and wastewater treatment: a review. Sep. Purif. Technol. **188**, 399–422 (2017). https://doi.org/10.1016/j.seppur.2017.07.015
34. J. Tong, L. Bo, Z. Li, Z. Lei, C. Xia, Magnetic $CoFe_2O_4$ nanocrystal: a novel and efficient heterogeneous catalyst for aerobic oxidation of cyclohexane. J. Mol. Catal. A Chem. **307**, 58–63 (2009). https://doi.org/10.1016/j.molcata.2009.03.010
35. T. Tsoncheva, E. Manova, N. Velinov, D. Paneva, M. Popova, B. Kunev, K. Tenchev, I. Mitov, Thermally synthesized nanosized copper ferrites as catalysts for environment protection. Catal. Commun. **12**, 105–109 (2010). https://doi.org/10.1016/j.catcom.2010.08.007
36. R. Benrabaa, A. Löfberg, A. Rubbens, E. Bordes-Richard, R.N. Vannier, A. Barama, Structure, reactivity and catalytic properties of nanoparticles of nickel ferrite in the dry reforming of methane. Catal. Today **203**, 188–195 (2013). https://doi.org/10.1016/j.cattod.2012.06.002
37. N. Rezlescu, E. Rezlescu, P.D. Popa, E. Popovici, C. Doroftei, M. Ignat, Preparation and characterization of spinel-type $MeFe_2O_4$ (Me = Cu, Cd, Ni and Zn) for catalyst applications. Mater. Chem. Phys. **137**, 922–927 (2013). https://doi.org/10.1016/j.matchemphys.2012.11.005
38. I. Popescu, A. Boudjemaa, N. Helaili, Y. Bessekhouad, M. Tudorache, K. Bachari, I.C. Marcu, Study of the electrical and catalytic properties of spinels with $CuFe_{2-x}Mn_xO_4$ composition (x = 0, 0.4, 0.8, 1.6 and 2). Appl. Catal. A Gen. **504**, 29–36 (2015). https://doi.org/10.1016/j.apcata.2014.09.048
39. Y. Wang, R. Xue, C. Zhao, F. Liu, C. Liu, F. Han, Effects of Ce in the catalytic combustion of toluene on $Cu_xCe_{1-x}Fe_2O_4$. Colloid Surf. A Physicochem. Eng. Asp. **540**, 90–97 (2018). https://doi.org/10.1016/j.colsurfa.2017.12.067
40. H. Zhang, R. Qi, D.G. Evans, X. Duan, Synthesis and characterization of a novel nano-scale magnetic solid base catalyst involving a layered double hydroxide supported on a ferrite core. J. Solid State Chem. **177**, 772–780 (2004). https://doi.org/10.1016/j.jssc.2003.09.009
41. T. Tatarchuk, B. Al-Najar, M. Bououdina, M.A. Aal Ahmed, Catalytic and photocatalytic properties of oxide spinels, in *Handbook of Ecomaterials*, ed. by L. M. Torres Martinez, O. V. Kharissova, B. I. Kharisov, vol. 3, (Springer, Cham, 2019), pp. 1701–1750. https://doi.org/10.1007/978-3-319-48281-1_158-1
42. D. Fino, S. Solaro, N. Russo, G. Saracco, V. Specchia, Catalytic removal of methane over thermal-proof nanostructured catalysts for CNG engines. Top. Catal. **42–43**, 449–454 (2007). https://doi.org/10.1007/s11244-007-0223-x
43. F. Papa, L. Patron, O. Carp, C. Paraschiv, I. Balint, Catalytic activity of neodymium substituted zinc ferrites for oxidative conversion of methane. J. Mol. Catal. A Chem. **299**, 93–97 (2009). https://doi.org/10.1016/j.molcata.2008.10.036
44. N. Velinov, K. Koleva, T. Tsoncheva, E. Manova, D. Paneva, K. Tenchev, B. Kunev, I. Mitov, Nanosized $Cu_{0.5}Co_{0.5}Fe_2O_4$ ferrite as catalyst for methanol decomposition: effect of preparation procedure. Catal. Commun. **32**, 41–46 (2013). https://doi.org/10.1016/j.catcom.2012.12.002
45. C. Trevisanut, M. Mari, J.M.M. Millet, F. Cavani, Chemical-loop reforming of ethanol over metal ferrites: an analysis of structural features affecting reactivity. Int. J. Hydrog. Energy **40**, 5264–5271 (2015). https://doi.org/10.1016/j.ijhydene.2015.01.054
46. H. Lee, J.C. Jung, H. Kim, Y.M. Chung, T.J. Kim, S.J. Lee, S.H. Oh, Y.S. Kim, I.K. Song, Preparation of $ZnFe_2O_4$ catalysts by co-precipitation method using aqueous buffer solution and their catalytic activity for oxidative dehydrogenation of n-butene to 1,3-butadiene. Catal. Lett. **122**, 281–286 (2008). https://doi.org/10.1007/s10562-007-9371-7

47. J.A. Toledo-Antonio, N. Nava, M. Martínez, X. Bokhimi, Correlation between the magnetism of non-stoichiometric zinc ferrites and their catalytic activity for oxidative dehydrogenation of 1-butene. Appl. Catal. A Gen. **234**, 137–144 (2002). https://doi.org/10.1016/S0926-860X(02)00212-0
48. D. Guin, B. Baruwati, S.V. Manorama, A simple chemical synthesis of nanocrystalline AFe_2O_4 (A = Fe, Ni, Zn): an efficient catalyst for selective oxidation of styrene. J. Mol. Catal. A Chem. **242**, 26–31 (2005). https://doi.org/10.1016/j.molcata.2005.07.021
49. P.P. Hankare, U.B. Sankpal, R.P. Patil, P.D. Lokhande, R. Sasikal, Synthesis, characterization and catalytic activity of chromium substituted cobalt ferrospinels. Mater. Sci. Eng. B Solid State Mater. Adv. Technol. **176**, 103–109 (2011). https://doi.org/10.1016/j.mseb.2010.10.005
50. M.M. Rashad, O.A. Fouad, Synthesis and characterization of nano-sized nickel ferrites from fly ash for catalytic oxidation of CO. Mater. Chem. Phys. **94**, 365–370 (2005). https://doi.org/10.1016/j.matchemphys.2005.05.028
51. O.A. Fouad, K.S. Abdel Halim, M.M. Rashad, Catalytic oxidation of CO over synthesized nickel ferrite nanoparticles from fly ash. Top. Catal. **47**, 61–65 (2008). https://doi.org/10.1007/s11244-007-9034-3
52. K.S. Abdel Halim, A.M. Ismail, M.H. Khedr, M.F. Abadir, Catalytic oxidation of CO gas over nanocrystallite $Cu_xMn_{1-x}Fe_2O_4$. Top. Catal. **47**, 66–72 (2008). https://doi.org/10.1007/s11244-007-9031-6
53. C.U. Aniz, T.D.R. Nair, A study on catalysis by ferrospinels for preventing atmospheric pollution from carbon monoxide. Open J. Phys. Chem. **1**, 124–130 (2011). https://doi.org/10.4236/ojpc.2011.13017
54. J.P. Jacobs, A. Maltha, J.G.H. Reintjes, J. Drimal, V. Ponec, H.H. Brongersma, The surface of catalytically active spinels. J. Catal. **147**, 294–300 (1994). https://doi.org/10.1006/jcat.1994.1140
55. R. Amrousse, T. Katsumi, Substituted ferrite $M_xFe_{1-x}Fe_2O_4$ (M = Mn, Zn) catalysts for N_2O catalytic decomposition processes. Catal. Commun. **26**, 194–198 (2012). https://doi.org/10.1016/j.catcom.2012.05.024
56. N. Hellaili, G. Mitran, I. Popescu, K. Bachari, I.C. Marcu, A. Boudjemaa, Photoelectrochemical properties of AFe_2O_4 (A = Co, Cu, Zn) ferrospinels for water photo-reduction. J. Electroanal. Chem. **742**, 47–53 (2015). https://doi.org/10.1016/j.jelechem.2015.01.018
57. A. Boudjemaa, I. Popescu, T. Juzsakova, M. Kebir, N. Helaili, K. Bachari, I.C. Marcu, M-substituted (M = Co, Ni and Cu) zinc ferrite photo-catalysts for hydrogen production by water photo-reduction. Int. J. Hydrog. Energy **41**, 11108–11118 (2016). https://doi.org/10.1016/j.ijhydene.2016.04.088
58. F. Li, J. Liu, D.G. Evans, X. Duan, Stoichiometric synthesis of pure MFe_2O_4 (M = Mg, Co and Ni) spinel ferrites from tailored layered double hydroxide (hydrotalcite-like) precursors. Chem. Mater. **16**, 1597–1602 (2004). https://doi.org/10.1021/cm035248c
59. J.B. Silva, C.F. Diniz, R.M. Lago, N.D.S. Mohallem, Catalytic properties of nanocomposites based on cobalt ferrites dispersed in sol-gel silica. J. Non-Cryst. Solids **348**, 201–204 (2004). https://doi.org/10.1016/j.jnoncrysol.2004.08.169
60. Y. Hammiche-Bellal, A. Benadda, L. Meddour-Boukhobza, S. Barama, A. Djadoun, A. Barama, Preparation and catalytic activity in ethanol combustion reaction of cobalt–iron spinel catalysts. Catal. Commun. **42**, 62–67 (2013). https://doi.org/10.1016/j.catcom.2013.07.042
61. R. Dumitru, F. Papa, I. Balint, D.C. Culita, C. Munteanu, N. Stanica, A. Ianculescu, L. Diamandescu, O. Carp, Mesoporous cobalt ferrite: a rival of platinum catalyst in methane combustion reaction. Appl. Catal. A Gen. **467**, 178–186 (2013). https://doi.org/10.1016/j.apcata.2013.07.013
62. A. Evdou, V. Zaspalis, L. Nalbandian, Ferrites as redox catalysts for chemical looping processes. Fuel **165**, 367–378 (2016). https://doi.org/10.1016/j.fuel.2015.10.049

63. T. Lazarova, D. Kovacheva, M. Georgieva, D. Tzankov, G. Tyuliev, I. Spassova, A. Naydenov, Tunable nanosized spinel manganese ferrites synthesized by solution combustion method. Appl. Surf. Sci. **496**, 143571 (2019). https://doi.org/10.1016/j.apsusc.2019.143571
64. J.E. Tasca, C.E. Quincoces, A. Lavat, A.M. Alvarez, M.G. González, Preparation and characterization of $CuFe_2O_4$ bulk catalysts. Ceram. Int. **37**, 803–812 (2011). https://doi.org/10.1016/j.ceramint.2010.10.023
65. Z.Y. Tian, P.M. Kouotou, A. El Kasmi, P.H.T. Ngamou, K. Kohse-Höinghaus, H. Vieker, A. Beyer, A. Gölzhäuser, Low-temperature deep oxidation of olefins and DME over cobalt ferrite. Proc. Combus. Inst. **35**, 2207–2214 (2015). https://doi.org/10.1016/j.proci.2014.06.111
66. N. Rezlescu, E. Rezlescu, P.D. Popa, C. Doroftei, M. Ignat, Some nanograined ferrites and perovskites for catalytic combustion of acetone at low temperature. Ceram. Int. **41**, 4430–4437 (2015). https://doi.org/10.1016/j.ceramint.2014.11.134
67. M. Florea, M. Alifanti, V.I. Parvulescu, D. Mihaila-Tarabasanu, L. Diamandescu, M. Feder, C. Negrila, L. Frunza, Total oxidation of toluene on ferrite-type catalysts. Catal. Today **141**, 361–366 (2009). https://doi.org/10.1016/j.cattod.2008.05.005
68. M.T. Rahman, C.V. Ramana, Impedance spectroscopic characterization of gadolinium substituted cobalt ferrite ceramics. J. Appl. Phys. **116**, 164108 (2014). https://doi.org/10.1063/1.4896945
69. S.J. Lee, C.C.H. Lo, P.N. Matlage, S.H. Song, Y. Melikhov, J.E. Snyder, D.C. Jiles, Magnetic and magnetoelastic properties of Cr-substituted cobalt ferrite. J. Appl. Phys. **102**, 073910 (2007). https://doi.org/10.1063/1.2794711
70. M.V. Chaudhari, S.E. Shirsath, A.B. Kadam, R.H. Kadam, S.B. Shelke, D.R. Mane, Site occupancies of Co–Mg–Cr–Fe ions and their impact on the properties of $Co_{0.5}Mg_{0.5}Cr_xFe_{2-x}O_4$. J. Alloy. Compd. **552**, 443–450 (2013). https://doi.org/10.1016/j.jallcom.2012.11.070
71. S.S. Ata-Allah, M.K. Fayek, H.S. Refai, M.F. Mostafa, Mössbauer effect study of copper containing nickel-aluminate ferrite. J. Solid State Chem. **149**, 434–442 (2000). https://doi.org/10.1006/jssc.1999.8577
72. A. Sutka, A. Borisova, J. Kleperis, G. Mezinskis, D. Jakovlev, I. Juhnevica, Effect of nickel addition on colour of nanometer spinel zinc ferrite pigments. J. Aust. Ceram. Soc. **48**, 150–155 (2012).
73. A. Khan, P.G. Smirniotis, Relationship between temperature-programmed reduction profile and activity of modified ferrite-based catalysts for WGS reaction. J. Mol. Catal. A Chem. **280**, 43–51 (2008). https://doi.org/10.1016/j.molcata.2007.10.022
74. A.S. Albuquerque, M.V.C. Tolentino, J.D. Ardisson, F.C.C. Moura, R. de Mendonça, W.A.A. Macedo, Nanostructured ferrites: structural analysis and catalytic activity. Ceram. Int. **38**, 2225–2231 (2012). https://doi.org/10.1016/j.ceramint.2011.10.071
75. V.L. Mathe, R.B. Kamble, Anomalies in electrical and dielectric properties of nanocrystalline Ni-Co spinel ferrite. Mater. Res. Bull. **43**, 2160–2165 (2008). https://doi.org/10.1016/j.materresbull.2007.09.001
76. R. Benrabaa, H. Boukhlouf, S. Barama, E. Bordes-Richard, R.N. Vannier, A. Barama, Structural, textural and acid-base properties of nano-sized $NiFe_2O_4$ spinel catalysts. Catal. Lett. **142**, 42–49 (2012). https://doi.org/10.1007/s10562-011-0726-8
77. N. Shukla, A. Ondeck, J.C. Lee, J.B. Miller, $NiFe_2O_4$@SiO_2 nanoparticles stabilized by porous silica shells. Catal. Lett. **142**, 582–587 (2012). https://doi.org/10.1007/s10562-012-0795-3
78. Y.J. Tu, C.K. Chang, C.F. You, Combustion of isopropyl alcohol using a green manufactured $CuFe_2O_4$. J. Hazard. Mater. **229-230**, 258–264 (2012). https://doi.org/10.1016/j.jhazmat.2012.05.100
79. J.T. Feng, Y.J. Lin, F. Li, D.G. Evans, D.Q. Li, Preparation, structure and properties of microspherical alumina with magnetic spinel ferrite cores. Appl. Catal. A Gen. **329**, 112–119 (2007). https://doi.org/10.1016/j.apcata.2007.06.032
80. B. Delmon, M. Devillers, Solid state reactions, in *Handbook of Heterogeneous Catalysis*, ed. by G. Ertl, H. Knozinger, F. Schuth, J. Weitkamp, 2nd edn., (Wiley-VCH, Weinheim, 2008), pp. 295–318

81. P. Lavela, J.L. Tirado, $CoFe_2O_4$ and $NiFe_2O_4$ synthesized by sol-gel procedures for their use as anode materials for Li ion batteries. J. Power Sources **172**, 379–387 (2007). https://doi.org/10.1016/j.jpowsour.2007.07.055
82. Y. Cheng, Y. Zheng, Y. Wang, F. Bao, Y. Qin, Synthesis and magnetic properties of nickel ferrite nano-octahedra. J. Solid State Chem. **178**, 2394–2397 (2005). https://doi.org/10.1016/j.jssc.2005.05.006
83. N. Rezlescu, E. Rezlescu, L. Sachelarie, P.D. Popa, C. Doroftei, Structural and catalytic properties of mesoporous nanocrystalline mixed oxides containing magnesium. Catal. Commun. **46**, 51–56 (2014). https://doi.org/10.1016/j.catcom.2013.11.021
84. V.R. Bhagwat, A.V. Humbe, S.D. More, K.M. Jadhav, Sol-gel auto combustion synthesis and characterizations of cobalt ferrite nanoparticles: different fuels approach. Mater. Sci. Eng. B Solid State Mater. Adv. Technol. **248**, 114388 (2019). https://doi.org/10.1016/j.mseb.2019.114388
85. Y. Li, E.R. Maxey, J.W. Richardson Jr., B. Ma, Structural and chemical evolution of Fe-Co-O based ceramics under reduction/oxidation—an in situ neutron diffraction study. Mater. Sci. Eng. B Solid State Mater. Adv. Technol. **106**, 6–26 (2004). https://doi.org/10.1016/j.mseb.2003.07.004
86. O. Carp, L. Patron, G. Pascu, I. Mindru, N. Stanica, Thermal investigations of nickel-zinc ferrites formation from malate coordination compounds. J. Therm. Anal. Calorim. **84**, 391–394 (2006). https://doi.org/10.1007/s10973-005-6920-4
87. J. Zhao, L. Mi, H. Hou, X. Shi, Y. Fan, The preparation of zinc ferrite nanorods by using single ferrocenyl complex as precursor. Mater. Lett. **61**, 4196–4198 (2007). https://doi.org/10.1016/j.matlet.2007.01.053
88. I.V. Vasylenko, K.S. Gavrylenko, V.G. Il'yin, V. Golub, G. Goloverda, V. Kolesnichenko, A.W. Addison, V.V. Pavlishchuk, The metamorphosis of heterometallic trinuclear antiferromagnetic complexes into nano-sized superparamagnetic spinels. Mater. Chem. Phys. **121**, 47–52 (2010). https://doi.org/10.1016/j.matchemphys.2009.12.040
89. B. Medina, M.G. Verdério Fressati, J.M. Gonçalves, F.M. Bezerra, F.A.P. Scacchetti, M.P. Moisés, A. Bail, R.B. Samulewski, Solventless preparation of Fe_3O_4 and Co_3O_4 nanoparticles: a mechanochemical approach. Mater. Chem. Phys. **226**, 318–322 (2019). https://doi.org/10.1016/j.matchemphys.2019.01.043
90. L. Leontie, C. Doroftei, Nanostructured spinel ferrites for catalytic combustion of gasoline vapors. Catal. Lett. **147**, 2542–2548 (2017). https://doi.org/10.1007/s10562-017-2164-8
91. C.H. Yan, Z.G. Xu, F.X. Cheng, Z.M. Wang, L.D. Sun, C.S. Liao, J.T. Jia, Nanophased $CoFe_2O_4$ prepared by combustion method. Solid State Commun. **111**, 287–291 (1999). https://doi.org/10.1016/S0038-1098(99)00119-2
92. V. Pillai, D.O. Shah, Synthesis of high-coercivity cobalt ferrite particles using water-in-oil microemulsions. J. Magn. Magn. Mater. **163**, 243–248 (1996). https://doi.org/10.1016/S0304-8853(96)00280-6
93. Y. Lee, J. Lee, C.J. Bae, J.G. Park, H.J. Noh, J.H. Park, T. Hyeon, Large-scale synthesis of uniform and crystalline magnetite nanoparticles using reverse micelles as nanoreactors under reflux conditions. Adv. Funct. Mater. **15**, 503–509 (2005). https://doi.org/10.1002/adfm.200400187
94. I. Spassova, M. Khristova, D. Panayotov, D. Mehandjiev, Coprecipitated CuO-MnO_x catalysts for low-temperature CO-NO and CO-NO-O_2 reactions. J. Catal. **185**, 43–57 (1999). https://doi.org/10.1006/jcat.1998.2347
95. G. Fierro, R. Dragone, G. Ferraris, NO and N_2O decomposition and their reduction by hydrocarbons over Fe-Zn manganite spinels. Appl. Catal. B Environ. **78**, 183–191 (2008). https://doi.org/10.1016/j.apcatb.2007.09.021
96. K. Zhi, Q. Liu, Y. Zhang, S. He, R. He, Effect of precipitator on the texture and activity of copper-manganese mixed oxide catalysts for the water gas shift reaction. J. Fuel Chem. Technol. **38**, 445–451 (2010). https://doi.org/10.1016/S1872-5813(10)60038-2

97. Y.H. Huang, S.F. Wang, A.P. Tsai, S. Kameoka, Reduction behaviors and catalytic properties for methanol steam reforming of Cu-based spinel compounds CuX_2O_4 (X= Fe, Mn, Al, La). Ceram. Int. **40**, 4541–4551 (2014). https://doi.org/10.1016/j.ceramint.2013.08.130
98. G.J. Hutchings, A.A. Mirzaei, R.W. Joyner, M.R.H. Siddiqui, S.H. Taylor, Effect of preparation conditions on the catalytic performance of copper manganese oxide catalysts for CO oxidation. Appl. Catal. A Gen. **166**, 143–152 (1998). https://doi.org/10.1016/S0926-860X(97)00248-2
99. B. Faure, P. Alphonse, Co-Mn-oxide spinel catalysts for CO and propane oxidation at mild temperature. Appl. Catal. B Environ. **180**, 715–725 (2016). https://doi.org/10.1016/j.apcatb.2015.07.019
100. J. Li, L. Li, F. Wu, L. Zhang, X. Liu, Dispersion-precipitation synthesis of nanorod Mn_3O_4 with high reducibility and the catalytic complete oxidation of air pollutants. Catal. Commun. **31**, 52–56 (2013). https://doi.org/10.1016/j.catcom.2012.11.013
101. C. Lahousse, A. Bernier, P. Grange, B. Delmon, P. Papaefthimiou, T. Ionnides, X. Verykios, Evaluation of γ-MnO_2 as a VOC removal catalyst: comparison with a noble metal catalyst. J. Catal. **178**, 214–225 (1998). https://doi.org/10.1006/jcat.1998.2148
102. M. Baldi, V.S. Escribano, J.M. Gallardo Amores, F. Milella, G. Busca, Characterization of manganese and iron oxides as combustion catalysts for propane and propene. Appl. Catal. B Environ. **17**, L175–L182 (1998). https://doi.org/10.1016/S0926-3373(98)00013-7
103. M. Piumetti, D. Fino, N. Russo, Mesoporous manganese oxides prepared by solution combustion synthesis as catalysts for the total oxidation of VOCs. Appl. Catal. B Environ. **163**, 277–287 (2015). https://doi.org/10.1016/j.apcatb.2014.08.012
104. S.C. Kim, W.G. Shim, Catalytic combustion of VOCs over a series of manganese oxide catalysts. Appl. Catal. B Environ. **98**, 180–185 (2010). https://doi.org/10.1016/j.apcatb.2010.05.027
105. Y. Wang, D. Yang, S. Li, L. Zhang, G. Zheng, L. Guo, Layered copper manganese oxide for the efficient catalytic CO and VOCs oxidation. Chem. Eng. J. **357**, 258–268 (2019). https://doi.org/10.1016/j.cej.2018.09.156
106. V.H. Vu, J. Belkouch, A. Ould-Dris, B. Taouk, Catalytic oxidation of volatile organic compounds on manganese and copper oxides supported on titania. AICHE J. **54**, 1585–1591 (2008). https://doi.org/10.1002/aic.11482
107. S. Behar, P. Gonzalez, P. Agulhon, F. Quignard, D. Świerczyński, New synthesis of nanosized Cu–Mn spinels as efficient oxidation catalysts. Catal. Today **189**, 35–41 (2012). https://doi.org/10.1016/j.cattod.2012.04.004
108. S.A. Hosseini, A. Niaei, D. Salari, S.R. Nabavi, Nanocrystalline AMn_2O_4 (A = Co, Ni, Cu) spinels for remediation of volatile organic compounds—synthesis, characterization and catalytic performance. Ceram. Int. **38**, 1655–1661 (2012). https://doi.org/10.1016/j.ceramint.2011.09.057
109. M.H. Castaño, R. Molina, S. Moreno, Cooperative effect of the Co-Mn mixed oxides for the catalytic oxidation of VOCs: influence of the synthesis method. Appl. Catal. A Gen. **492**, 48–59 (2015). https://doi.org/10.1016/j.apcata.2014.12.009
110. D.B. Ghare, A.P.B. Sinha, L. Singh, Change in the valency state of ions in $CuMn_2O_4$ at high temperatures. J. Mater. Sci. **2**, 389–394 (1968). https://doi.org/10.1007/BF00550982
111. B. Gillot, S. Buguet, E. Kester, Oxidation mechanism and valence states of copper and manganese in tetragonal $CuMn_2O_4$. J. Mater. Chem. **7**, 2513–2517 (1997). https://doi.org/10.1039/a703731g
112. T. Valdés-Solis, I. López, G. Marban, Copper manganite as a catalyst for the PROX reaction. Deactivation studies. Int. J. Hydrog. Energy **35**, 1879–1887 (2010). https://doi.org/10.1016/j.ijhydene.2009.12.117
113. Z. Ye, J.M. Giraudon, N. Nuns, P. Simon, N. De Geyter, R. Morent, J.F. Lamonier, Influence of the preparation method on the activity of copper-manganese oxides for toluene total oxidation. Appl. Catal. B Environ. **223**, 154–166 (2018). https://doi.org/10.1016/j.apcatb.2017.06.072

114. C. Dong, Z. Qu, Y. Qin, Q. Fu, H. Sun, X. Duan, Revealing the highly catalytic performance of spinel $CoMn_2O_4$ for toluene oxidation: involvement and replenishment of oxygen species using in situ designed-TP techniques. ACS Catal. **9**, 6698–6710 (2019). https://doi.org/10.1021/acscatal.9b01324
115. W. Tang, X. Wu, S. Li, W. Li, Y. Chen, Porous Mn-Co mixed oxide nanorod as a novel catalyst with enhanced catalytic activity for removal of VOCs. Catal. Commun. **56**, 134–138 (2014). https://doi.org/10.1016/j.catcom.2014.07.023
116. S. Behar, N.A. Gómez-Mendoza, M.Á. Gómez-García, D. Świerczyński, F. Quignard, N. Tanchoux, Study and modelling of kinetics of the oxidation of VOC catalyzed by nanosized Cu-Mn spinels prepared via an alginate route. Appl. Catal. A Gen. **504**, 203–210 (2015). https://doi.org/10.1016/j.apcata.2014.12.021
117. Y. Huang, K. Ye, H. Li, W. Fan, F. Zhao, Y. Zhang, H. Ji, A highly durable catalyst based on $Co_xMn_{3-x}O_4$ nanosheets for low-temperature formaldehyde oxidation. Nano Res. **9**, 3881–3892 (2016). https://doi.org/10.1007/s12274-016-1257-9
118. X. Wang, W. Zhao, X. Wu, T. Zhang, Y. Liu, K. Zhang, Y. Xiao, L. Jiang, Total oxidation of benzene over ACo_2O_4 (A = Cu, Ni and Mn) catalysts: In situ DRIFTS account for understanding the reaction mechanism. Appl. Surf. Sci. **426**, 1198–1205 (2017). https://doi.org/10.1016/j.apsusc.2017.07.269
119. Z. Chen, S. Wang, W. Liu, X. Gao, D. Gao, M. Wang, S. Wang, Morphology-dependent performance of Co_3O_4 via facile and controllable synthesis for methane combustion. Appl. Catal. A Gen. **525**, 94–102 (2016). https://doi.org/10.1016/j.apcata.2016.07.009
120. Z. Fan, W. Fang, Z. Zhang, M. Chen, W. Shangguan, Highly active rod-like Co_3O_4 catalyst for the formaldehyde oxidation reaction. Catal. Commun. **103**, 10–14 (2018). https://doi.org/10.1016/j.catcom.2017.09.003
121. T. Garcia, S. Agouram, J.F. Sánchez-Royo, R. Murillo, A.M. Mastral, A. Aranda, I. Vázquez, A. Dejoz, B. Solsona, Deep oxidation of volatile organic compounds using ordered cobalt oxides prepared by a nanocasting route. Appl. Catal. A Gen. **386**, 16–27 (2010). https://doi.org/10.1016/j.apcata.2010.07.018
122. J. Mei, J. Xie, Z. Qu, Y. Ke, X. Hu, N. Yan, Ordered mesoporous spinel Co_3O_4 as a promising catalyst for the catalytic oxidation of dibromomethane. Mol. Catal. **461**, 60–66 (2018). https://doi.org/10.1016/j.mcat.2018.10.001
123. Y. Zheng, Y. Liu, H. Zhou, W. Huang, Z. Pu, Complete combustion of methane over Co_3O_4 catalysts: influence of pH values. J. Alloy. Compd. **734**, 112–120 (2018). https://doi.org/10.1016/j.jallcom.2017.11.008
124. W. Zhang, F. Wu, J. Li, Z. You, Dispersion–precipitation synthesis of highly active nanosized Co_3O_4 for catalytic oxidation of carbon monoxide and propane. Appl. Surf. Sci. **411**, 136–143 (2017). https://doi.org/10.1016/j.apsusc.2017.03.162
125. J. Łojewska, A. Kołodziej, T. Łojewski, R. Kapica, J. Tyczkowski, Structured cobalt oxide catalyst for VOC combustion. Part I: catalytic and engineering correlations. Appl. Catal. A Gen. **366**, 206–211 (2009). https://doi.org/10.1016/j.apcata.2009.07.006
126. H. Biederman, *Plasma Polymer Films* (Imperial College Press, London, 2004). https://doi.org/10.1142/p336
127. J. Tyczkowski, R. Kapica, J. Łojewska, Thin cobalt oxide films for catalysis deposited by plasma-enhanced metal-organic chemical vapor deposition. Thin Solid Films **515**, 6590–6595 (2007). https://doi.org/10.1016/j.tsf.2006.11.056
128. J. Łojewska, A. Kolodziej, R. Kapica, A. Knapik, J. Tyczkowski, In search for active non-precious metal catalyst for VOC combustion. Evaluation of plasma deposited Co and Co/Cu oxide catalysts on metallic structured carriers. Catal. Today **147S**, S94–S98 (2009). https://doi.org/10.1016/j.cattod.2009.07.021
129. D.K. Chlebda, P.J. Jodłowski, R.J. Jędrzejczyk, J. Łojewska, 2D-COS of in situ μ-Raman and in situ IR spectra for structure evolution characterisation of NEP-deposited cobalt oxide catalyst during n-nonane combustion. Spectrochim. Acta A Mol. Biomol. Spectrosc. **186**, 44–51 (2017). https://doi.org/10.1016/j.saa.2017.06.009

130. M.C. Petty, *Langmuir-Blodgett Films: An Introduction* (Cambridge University Press, Cambridge, 1996). https://doi.org/10.1002/adma.19970091019
131. J. Łojewska, P. Dynarowicz-Łatka, A. Kołodziej, Preparation, characterization and deposition of Langmuir-Blodgett Co, Al organic films for the catalytic applications. Thin Solid Films **495**, 299–307 (2006). https://doi.org/10.1016/j.tsf.2005.08.202
132. S. Deb, S. Biswas, S.A. Hussain, D. Bhattacharjee, Spectroscopic characterizations of the mixed Langmuir-Blodgett (LB) films of 2,20-biquinoline molecules: Evidence of dimer formation. Chem. Phys. Lett. **405**, 323–329 (2005). https://doi.org/10.1016/j.cplett.2005.02.060
133. P.J. Jodłowski, R.J. Jędrzejczyk, D. Chlebda, J. Tyczkowsk, J. Kryca, A. Kołodziej, J. Łojewska, Structure effects on activity of plasma deposited cobalt oxide catalysts for VOC combustion. Top. Catal. **60**, 318–325 (2017). https://doi.org/10.1007/s11244-016-0618-7
134. Q. Wang, Y. Peng, J. Fu, G.Z. Kyzas, S.M.R. Billah, S. An, Synthesis, characterization, and catalytic evaluation of Co_3O_4/γ-Al_2O_3 as methane combustion catalysts: significance of Co species and the redox cycle. Appl. Catal. B Environ. **168-169**, 42–50 (2015). https://doi.org/10.1016/j.apcatb.2014.12.016
135. B. Xiao, K. Zhao, L. Zhang, T. Cai, X. Zhang, Z. Wang, J. Yuan, L. Yang, P. Gao, D. He, A green and facile synthesis of Co_3O_4 monolithic catalyst with enhanced total oxidation of propane performance. Catal. Commun. **116**, 1–4 (2018). https://doi.org/10.1016/j.catcom.2018.07.013
136. T.H. Lim, S.B. Park, J.M. Kim, D.H. Kim, Ordered mesoporous MCo_2O_4 (M = Cu, Zn and Ni) spinel catalysts with high catalytic performance for methane combustion. J. Mol. Catal. A Chem. **426**, 68–74 (2017). https://doi.org/10.1016/j.molcata.2016.11.002
137. C. Zhang, J. Wang, S. Yang, H. Liang, Y. Men, Boosting total oxidation of acetone over spinel MCo_2O_4 (M = Co, Ni, Cu) hollow mesoporous spheres by cation-substituting effect. J. Colloid Interf. Sci. **539**, 65–75 (2019). https://doi.org/10.1016/j.jcis.2018.12.061
138. Z. Pu, Y. Liu, H. Zhou, W. Huang, Y. Zheng, X. Li, Catalytic combustion of lean methane at low temperature over ZrO_2-modified Co_3O_4 catalysts. Appl. Surf. Sci. **422**, 85–93 (2017). https://doi.org/10.1016/j.apsusc.2017.05.231
139. S.A. Hosseini, A. Niaei, D. Salari, M.C. Alvarez-Galvan, J.L.G. Fierro, Study of correlation between activity and structural properties of Cu-(Cr, Mn and $Co)_2$ nano mixed oxides in VOC combustion. Ceram. Int. **40**, 6157–6163 (2014). https://doi.org/10.1016/j.ceramint.2013.11.068